Refined physical parameters for Chariklo's body and rings from stellar occultations observed between 2013 and 2020

81 authors, including:

Bruno Eduardo Morgado
Observatório Nacional
37 PUBLICATIONS   **267** CITATIONS

SEE PROFILE

Bruno Sicardy
Observatoire de Paris
420 PUBLICATIONS   **7,233** CITATIONS

SEE PROFILE

Felipe Braga-Ribas
Federal University of Technology - Paraná/Brazil (UTFPR)
120 PUBLICATIONS   **1,386** CITATIONS

SEE PROFILE

J. Desmars
Institut de Mécanique Céleste et de Calcul des Éphémérides
93 PUBLICATIONS   **902** CITATIONS

SEE PROFILE

Some of the authors of this publication are also working on these related projects:

Project Stellar occultations View project

Project DEVELOPMENT OF HIGH RESOLUTION SPECTROSCOPY TECHNIQUES FOR ASTRONOMY View project

Refined physical parameters for Chariklo's body and rings from stellar occultations observed between 2013 and 2020

B. E. Morgado[1,2,3], B. Sicardy[1], F. Braga-Ribas[4,3,2,1], J. Desmars[5,6,1], A. R. Gomes-Júnior[7,2], D. Bérard[1], R. Leiva[8,9,1], J. L. Ortiz[10], R. Vieira-Martins[3,2,11], G. Benedetti-Rossi[1,2,7], P. Santos-Sanz[10], J. I. B. Camargo[3,2], R. Duffard[10], F. L. Rommel[3,2,4], M. Assafin[11,2], R. C. Boufleur[2,3], F. Colas[6], M. Kretlow[12,10,13], W. Beisker[12,13], R. Sfair[7], C. Snodgrass[14], N. Morales[10], E. Fernández-Valenzuela[15], L. S. Amaral[16], A. Amarante[17], R. A. Artola[18], M. Backes[19,20], K-L. Bath[12,13], S. Bouley[21], M. W. Buie[22], P. Cacella[23], C. A. Colazo[24], J. P. Colque[25], J-L. Dauvergne[26], M. Dominik[27], M. Emilio[28,3], C. Erickson[29], R. Evans[19], J. Fabrega-Polleri[30], D. Garcia-Lambas[18], B. L. Giacchini[31,32], W. Hanna[33], D. Herald[12,33], G. Hesler[34], T. C. Hinse[35,36], C. Jacques[37], E. Jehin[38], U. G. Jørgensen[39], S. Kerr[33,40], V. Kouprianov[41,42], S. E. Levine[43,44], T. Linder[45], P. D. Maley[46,47], D. I. Machado[48,49], L. Maquet[6], A. Maury[50], R. Melia[18], E. Meza[1,51,52], B. Mondon[34], T. Moura[7], J. Newman[33], T. Payet[34], C. L. Pereira[4,3,2], J. Pollock[53], R. C. Poltronieri[54,16], F. Quispe-Huaynasi[3], D. Reichart[41], T. de Santana[1,7], E. M. Schneiter[18], M. V. Sieyra[55], J. Skottfelt[56], J. F. Soulier[57], M. Starck[58], P. Thierry[59], P. J. Torres[60,61], L. L. Trabuco[49], E. Unda-Sanzana[25], T. A. R. Yamashita[7], O. C. Winter[7], A. Zapata[62,63], and C. A. Zuluaga[44]

(Affiliations can be found after the references)

ABSTRACT

Context. The Centaur (10199) Chariklo has the first rings system discovered around a small object. It was first observed using stellar occultation in 2013. Stellar occultations allow the determination of sizes and shapes with kilometre accuracy and obtain characteristics of the occulting object and its vicinity.

Aims. Using stellar occultations observed between 2017 and 2020, we aim at constraining Chariklo's and its rings physical parameters. We also determine the rings' structure, and obtain precise astrometrical positions of Chariklo.

Methods. We predicted and organised several observational campaigns of stellar occultations by Chariklo. Occultation light curves were measured from the data sets, from which ingress and egress times, and rings' width and opacity were obtained. These measurements, combined with results from previous works, allow us to obtain significant constraints on Chariklo's shape and rings' structure.

Results. We characterise Chariklo's ring system (C1R and C2R), and obtain radii and pole orientations that are consistent with, but more accurate than, results from previous occultations. We confirmed the detection of W-shaped structures within C1R and an evident variation of radial width. The observed width ranges between 4.8 and 9.1 km with a mean value of 6.5 km. One dual observation (visible and red) does not reveal any differences in the C1R opacity profiles, indicating ring particle's size larger than a few microns. The C1R ring eccentricity is found to be smaller than 0.022 (3σ), and its width variations may indicate an eccentricity higher than ~0.005. We fit a tri-axial shape to Chariklo's detections over eleven occultations and determine that Chariklo is consistent with an ellipsoid with semi-axes of $143.8^{+1.4}_{-1.5}$, $135.2^{+1.4}_{-2.8}$ and $99.1^{+5.4}_{-2.7}$ km. Ultimately, we provided seven astrometric positions at a milliarcseconds accuracy level, based on Gaia EDR3, and use it to improve Chariklo's ephemeris.

Key words. Occultations – Methods: observational – Methods: data analysis – Minor planets, asteroids: individual: Chariklo – Planets and satellites: rings

1. Introduction

The Centaur (10199) Chariklo is a small object in our Solar System moving on an elliptical orbit between Saturn and Uranus, at heliocentric distances varying from 13.1 to 18.9 au. It was discovered in 1997 (Ticha et al. 1997), it is the largest Centaur known to date. From thermal infrared observations, its surface equivalent radius ranges between 109 and 151 km (Jewitt & Kalas 1998; Altenhoff et al. 2001; Campins & Fernández 2002; Sekiguchi et al. 2012; Bauer et al. 2013; Fornasier et al. 2013, 2014; Lellouch et al. 2017), with a most recent solution of 121 ± 4 km (Lellouch et al. 2017) obtained with the Atacama Large Millimeter/submillimeter Array (ALMA[1]).

From a stellar occultation observed in 2013, Braga-Ribas et al. (2014) reported the discovery of two dense and narrow

rings (named 2013C1R and 2013C2R, C1R and C2R for short) surrounding Chariklo at 390 and 405 km from the body centre, respectively. This was the first time that rings were observed elsewhere than around giant planets. Being narrow and dense, they bear resemblance with some of Uranus' rings (Elliot et al. 1984; French et al. 1991). More on Chariklo's rings properties (orbital radii and pole, width and opacity) is given by Bérard et al. (2017) and are reviewed in Sicardy et al. (2018).

Another ring was later-on discovered around the dwarf planet (136108) Haumea (Ortiz et al. 2017), and there are evidences (yet to be confirmed) of a ring (or a dust shell) around the Centaur (2060) Chiron (Ortiz et al. 2015; Sickafoose et al. 2020). This raises new questions on these ring systems origins, dynamical evolution and stability, and this has been studied by several authors, see for example Pan & Wu (2016); Hyodo et al. (2016); Melita et al. (2017); Michikoshi & Kokubo (2017); Araujo et al.

---

[1] https://www.almaobservatory.org/en/home/

(2018); Sicardy et al. (2018, 2019) and references therein. Dynamical models are essential to address these questions and better understand the orbital evolution of ring particles around these small objects. On the other hand, new observations can be used to constrain these dynamical models and provide new insights into the origin and evolution of rings around small bodies.

Chariklo's ring system has a diameter of ~800 km, subtending about 80 milliarcseconds (mas) when projected onto the sky plane as seen from Earth. As a consequence, resolved ground-based imaging of this system is extremely challenging with currently available equipment. For instance, Sicardy et al. (2015) observed this system with the SPHERE, an Adaptive Optics system attached at the 8.2-m Very Large Telescope (VLT/ESO) and obtained Point Spread Function (PSFs) of 30-40 mas (corresponding to ~300-400 km at Chariklo's distance). These authors also observed the system with the Hubble Space Telescope (HST), with typical PSFs of 30 mas. None of those observations were able to detect Chariklo's rings, or find an extended system of cometary jets or tenuous dust around the body. In contrast, stellar occultations can achieve resolutions at km-level and provide stringent constraints on the size and shape of the main body and its astrometric position at mas level. Moreover, optical depths and inner structures of the rings can be revealed.

Between 2013 and 2016, thirteen stellar occultations by Chariklo's system were observed, from those only the occultation of 2013-06-03 (Braga-Ribas et al. 2014; Bérard et al. 2017) has more than two chords detections over C1R. As there was no occultation with three or more detections of the main body, Leiva et al. (2017) used five of single-chord and double-chords occultations to derive possibles 3D shapes of Chariklo's main body. Bérard et al. (2017) mentions that a two-chord occultation by CR1 was observed from Australia on 2016-10-01, see Fig. 3 of that paper. This event was also a two-chord on the main body, and used by Leiva et al. (2017).

These authors derived four possible solutions for Chariklo's shape: (*i*) a sphere with radius $R = 129 \pm 3$ km; (*ii*) a Maclaurin spheroid with semi-axes $a = b = 143^{+3}_{-6}$ km and $c = 96^{+14}_{-4}$ km; (*iii*) a Jacobi ellipsoid with $a = 157 \pm 4$ km, $b = 139 \pm 4$ km and $c = 86 \pm 1$ km; and (*iv*) a triaxial ellipsoid with $a = 148^{+6}_{-4}$ km, $b = 132^{+6}_{-5}$ km and $c = 102^{+10}_{-8}$ km.

Bérard et al. (2017) confirmed the presence of Chariklo's rings and their geometry as published by Braga-Ribas et al. (2014). Moreover, they provided for the first time resolved opacity profiles of CR1, revealing a W-shaped structure, and found significant azimuthal width variations for that ring, with values ranging between 5.0 and 7.5 km. This is reminiscent of the ring width variations found among Uranus' dense rings, in particular its widest one, the ϵ ring (Nicholson et al. 2018).

In this paper, we present the results of eight unpublished stellar occultations by Chariklo and its ring system observed between 2017 and 2020. It contains the analysis of three multi-chord detections of Chariklo's main body, two multi-chord detections of C1R and one multi-chord detection of C2R. The parameters obtained here can be used to further constrain the dynamical models of the rings, and the size and shape of Chariklo.

In Section 2 we describe our prediction process and the observational campaigns. Section 3 details the reduction process. In Section 4 we present our results concerning Chariklo's rings, with the estimation of pole orientation (4.1), C1R structures and global parameters (4.2.1) and C2R global parameters (4.3). Section 5 contains the analysis of Chariklo's 3D shape considering 11 stellar occultation chords obtained between 2013 and 2020. In Section 6 we present Chariklo's astrometric solution derived from our work. Conclusions are provided in Section 7.

2. Predictions and Observational Campaigns

All the events presented here were predicted in the framework of the European Research Council (ERC) *Lucky Star* project[2], and are publicly available for the community. After 2016, the Gaia DR1 (GDR1) catalogue (Gaia Collaboration et al. 2016b,a) was the source of the stellar positions for our prediction pipeline (Assafin et al. 2012; Camargo et al. 2014; Desmars et al. 2015). After December 2018, it was replaced by the Gaia DR2 (GDR2) catalogue (Gaia Collaboration et al. 2018), and by Gaia EDR3 (GEDR3) after the beginning of 2021 (Gaia Collaboration et al. 2021). Regular astrometric programs were carried out at the European Southern Observatory (ESO), the Observatório do Pico dos Dias (OPD/LNA) and the Observatorio de Sierra Nevada (OSN), among others, to improve the ephemerides of various objects.

Selected events triggered observational campaigns, involving both fixed and portable telescopes that were deployed along the predicted shadow paths. Besides professional astronomers, they also involved citizen astronomer communities, such as the International Occultation Timing Association (IOTA/Europe[3]), Planoccult[4], and Occult Watcher[5].

Chariklo's ephemeris was pinned down to the five-milliarcsec (mas) level (~50 km at Chariklo's distance, Desmars et al. 2017) using previous stellar occultations published by Braga-Ribas et al. (2014); Leiva et al. (2017); Bérard et al. (2017), GDR2, and the NIMA (Numerical Integration of the Motion of an Asteroid Desmars et al. 2015) integrator. This uncertainty, being smaller than the size of Chariklo, allowed the detection of multi-chord stellar occultations by Chariklo and its rings between 2017 and 2020.

Table 1 provides information related to the observed events. It lists the geocentric closest approach time (UTC), the Gaia EDR3 source identifier, the geocentric ICRS coordinates of the stars at occultation epoch, applying proper motion, parallax, and radial velocity (when available). The last column of the table lists the (Gaia) G magnitude of the stars, which can be compared to Chariklo's V magnitude, ~18.9.

Our campaigns involved sites in South and North America, Africa, and Oceania. The observations used a wide range of telescope sizes, from small portable telescopes (0.25-0.30 m) to large observatories facilities such as the Very Large Telescope (VLT, 8.20 m), Gemini North (8.10 m), Southern Astrophysical Research (SOAR, 4.10 m), Observatório Pico dos Dias (OPD, 1.60 m), and Danish/ESO (1.54 m). The observational circumstances (telescopes, instruments, stations, observers, etc.) are given in Appendix A.

3. Data Analysis

We used classical photometric pipelines to extract the occultation light curves, as detailed in Section 3.1. Abrupt opaque edges models, including the effects of diffraction, finite band width, exposure time and stellar diameter, were fitted to the star dis- and re-appearances behind Chariklo's main body. For ring occultations, the apparent opacity is also an adjustable parameter. The timings obtained at the various stations define occultation chords, that are in turn used to constrain Chariklo's shape (Section 3.2) and the ring size and orientation is space (Section 3.3).

---

[2] https://lesia.obspm.fr/lucky-star/index.php
[3] https://www.iota-es.de/
[4] http://vps.vvs.be/mailman/listinfo/planoccult
[5] https://www.occultwatcher.net/

Table 1. Occulted stars parameters for each observed event as obtained from Gaia EDR3.

Occ. date and time UTC	Gaia EDR3 source identifier	Right Ascension[1]	Declination[1]	G mag
2020-06-19 15:51	6852214948874014720	$20^h\,02^m\,31^s.99612 \pm 0.21$ mas	-22° 20' 41".4784 $\pm$ 0.14 mas	15.569
2019-09-04 08:03	6766511277365829760	$19^h\,27^m\,42^s.15144 \pm 0.09$ mas	-25° 29' 21".2488 $\pm$ 0.06 mas	13.117
2019-08-08 21:41	6766365630734160896	$19^h\,31^m\,49^s.78464 \pm 0.11$ mas	-25° 34' 26".7724 $\pm$ 0.09 mas	15.158
2019-08-02 10:02	6766356933423996544	$19^h\,33^m\,07^s.47470 \pm 0.42$ mas	-25° 34' 42".3668 $\pm$ 0.35 mas	17.766
2017-08-24 02:59	6737213175138988672	$18^h\,42^m\,35^s.22729 \pm 0.18$ mas	-31° 09' 50".6837 $\pm$ 0.14 mas	17.468
2017-07-23 05:58	6737020112089260672	$18^h\,48^m\,09^s.22138 \pm 0.04$ mas	-31° 26' 32".4591 $\pm$ 0.03 mas	14.005
2017-06-22 21:18	6760223758801661440	$18^h\,55^m\,15^s.65251 \pm 0.04$ mas	-31° 31' 21".6706 $\pm$ 0.03 mas	14.223
2017-04-09 02:24	6757456459825426560	$19^h\,04^m\,03^s.62801 \pm 0.03$ mas	-31° 17' 15".2304 $\pm$ 0.03 mas	14.094

[1] The stars coordinates (RA and Dec.) and their uncertainties were propagated to the occultation epoch with the formalism proposed by Butkevich & Lindegren (2014) using the parameters (proper motion, parallax, radial velocity, etc) from Gaia EDR3 (Gaia Collaboration et al. 2021).

3.1. Calibration and aperture photometry

All the images were converted to the standard `fits` format. The video files (`ser` or `avi`) were converted using TANGRA v3.7.3 (Pavlov 2020) or Python codes based on ASTROPY v4.0.1 (Astropy Collaboration et al. 2013). When available, calibration images (bias, dark and flat-field) were used to correct the original images using standard IRAF (Image Reduction and Analysis Facility Butcher & Stevens 1981) procedures.

The flux from the target stars was obtained by aperture photometry using the PRAIA (Platform for Reduction of Astronomical Images Automatically Assafin et al. 2011) package. Note that during the occultation, the star and Chariklo images are blended together in the same aperture. The total flux from the star and Chariklo was normalised to unity outside the occultation, using a polynomial fit just before and after the event. Finally, nearby stars were used as photometric calibrators to correct for low-frequency sky transparency fluctuations. The resulting light curves are displayed in Appendix F.

3.2. Times and projection in the sky plane

The immersion (t_{imm}) and emersion (t_{eme}) times were determined using a Monte Carlo approach with uniformly distributed parameters to test a vast number of simulated models (∼100,000) for which chi-squared statistics are computed. This was done with the SORA v0.1.2 (Stellar Occultation Reduction Analysis)[6] package. The models consider a sharp-edge occultation model convolved with Fresnel diffraction, apparent stellar diameter (at Chariklo's distance), and finite integration time. For more details, see Braga-Ribas et al. (2013) and references therein.

To determine the rings' parameters, we also need to fit the apparent opacity (p') of the flux drop (Bérard et al. 2017). If insufficiently sampled, there is a large correlation between the apparent opacity of the rings and the duration of the detection ($\Delta t = t_{eme} - t_{imm}$). Thus, the positive ring detections have been divided into two groups: resolved detections, with more than three points showing a significant stellar flux drop during the occultation (higher than 3σ); and unresolved detections, with less than three significant points. The three parameters (t_{imm}, t_{eme} and p') can be fitted for the resolved detections, while the unresolved detections allow only the unambiguous determination of the cen-

tral time ($t_{mean} = \frac{1}{2}(t_{eme} - t_{imm})$). The obtained parameters for the main body and rings are listed in Tables C.1 and C.1, and an example of analysed light curve is provided in Fig. 1.
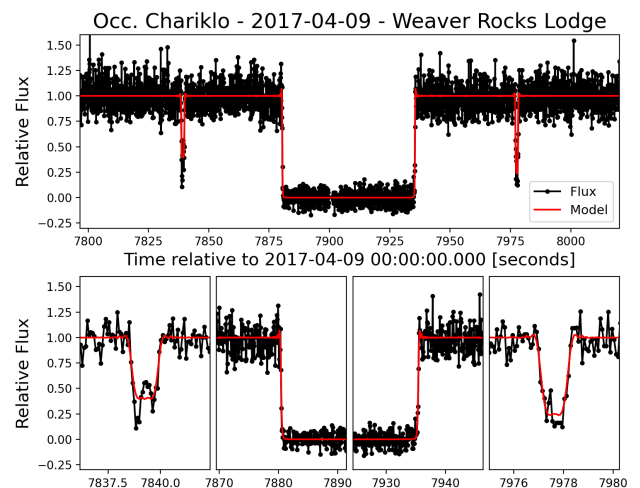
Fig. 1. Normalised light curve obtained at Weaver Rocks Lodge on 2017-04-09. The black dots show the observational data, while the red lines represent the fitted model. The bottom panels contain a zoom of 20 seconds centred on the immersion and emersion times and 2.5 seconds centred in each C1R detection. In this data-set, there is no clear detection of C2R. All the light curves of this work can be found in Appendix F.

Using Chariklo ephemeris (NIMA v.17), the GEDR3 stars' position propagated to the event epoch and the observer's position on Earth (latitude, longitude, and height), each occultation time is associated with a stellar position relative to Chariklo (f, g), as projected in the sky plane. The position (f, g) is expressed in kilometers, f (resp. g) being counted positively towards the local east (resp. north) celestial direction. Note that an offset in right ascension and declination, (f_0, g_0), must be applied to Chariklo's ephemeris to account for errors on both the ephemeris and the star position. This point is discussed in the sub-section 3.3. Thus, the final Chariklo-centric stellar position in the sky plane is given by ($f - f_0$, $g - g_0$). Those positions are used in turn

---

[6] Website: https://sora.readthedocs.io/

to determine Chariklo's rings orbital parameters and Chariklo's size and shape, see Sections 4 and 5.

3.3. Projection in the ring plane

The ring parameters obtained in the sky-plane (as derived from t_{imm}, t_{eme} and p') are projected in the ring plane to derive the relevant parameters, more precisely: (*i*) the ring radial width W_r; (*ii*) its distance r to Chariklo's centre; and (*iii*) its normal opacity, p_N. The quantities W_r and r are calculated by projecting the corresponding $(f - f_0, g - g_0)$ in the ring plane, once the ring pole orientation (α_p, δ_p) is known.

Finally, the ring opacity normal to its plane, p_N, is given by

$$p_N = p' \, . \, |\sin(B)|, \tag{1}$$

assuming a monolayer disk, where B is the ring opening angle ($B = 0°$ and $B = 90°$ corresponding to edge-on and pole-on viewings, respectively).

A relevant integral quantity can also be derived, the equivalent width ($E_p = W_r \, . \, p_N$), which is related to the amount of material present in a radial cut of the ring. General discussions concerning those parameters are provided in Elliot et al. (1984); French et al. (1991), and a more specific application to Chariklo's ring is presented in Bérard et al. (2017). The derived ring parameters are listed in Tables C.2-C.2.

4. Rings' structures and parameters

4.1. Ring Pole

From the multi-chord ring detection of 2013-06-03, Braga-Ribas et al. (2014) derived two possible ring pole orientations, assuming the ring to be circular. In that case, the apparent ring oblateness ϵ' projected in the sky plane is given by

$$\epsilon' = 1 - \sin(B). \tag{2}$$

Long-term photometric trends (Duffard et al. 2014) allowed to remove this ambiguity, providing $\alpha_p = 10^h \, 05^m \pm 2^m$ and $\delta_p = +41° \, 29' \pm 13'$. This solution was later confirmed by stellar occultations observed between 2014 and 2016 (Bérard et al. 2017). Note that the ring pole orientation is in principle defined as being in the direction of the ring angular momentum, which in turn depends on the (unknown) direction of motion for the ring particles. This allows the possible solution $\alpha_p + 180°$ and $-\delta_p$. Here, we choose arbitrarily the solution with $\delta_p > 0$. This choice can be modified when the direction of motion is known, and do not influence our results.

The ring orbital parameters are obtained by fitting an ellipse to the occultation points, as seen in the sky plane. Five parameters are adjusted: the centre of the ellipse (f_0, g_0); the apparent semi-major axis (a'); the apparent oblateness $(\epsilon' = 1 - b'/a')$; and the position angle (P) of the apparent semi-minor axis (b'), counted positively from the celestial north direction towards the celestial east.

In this work, and to avoid underdetermined fits, we only consider the occultations which have at least six C1R detections, plus the discovery observation on 2013. These events were observed on 2017-06-22 and 2017-07-23, and are used to pin down the pole orientation and assess possible ring eccentricities.

The fit uses a Monte Carlo approach with uniformly distributed parameters to test ~10,000,000 ellipses, thus providing a χ^2 statistics, as well as the best fit corresponding to the minimum value, χ^2_{min}. The range χ^2_{min} to $\chi^2_{\text{min}} + 1$ then provides the

marginal 1σ error bar for each parameter, i.e. the 68.3% confidence for that parameter, ignoring the other four parameters, see Souami et al. (2020) and references therein for more details. In this project, this step was done with the SORA v0.1.2 package.

Assuming that C1R is circular with radius r_{C1R} equals the fitted a', we derive the pole orientation (α_p, δ_p) from B and P, using the equations
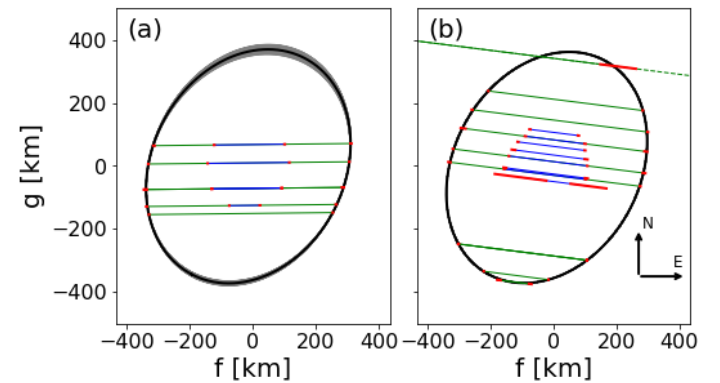
$$\sin(\delta_p) = \cos(B)\cos(P)\cos(\delta) - \sin(B)\sin(\delta), \tag{3}$$
$$\cos(\alpha - \alpha_p) = -[\sin(B) + \sin(\delta)\sin(\delta_p)]/[\cos(\delta)\cos(\delta_p)], \tag{4}$$
$$\sin(\alpha - \alpha_p) = -\cos(B)\sin(P)/\cos(\delta_p), \tag{5}$$

where (α, δ) is Chariklo's ICRS position at epoch.

Figure 2 displays the best-fitted ellipse on C1R for the events on 2017-06-22 and 2017-07-23. It also shows the sky-plane projection of the obtained chords of the main body and rings. The obtained values are given in Table 2.

Fig. 2. Chords in the sky-plane relative to Chariklo's main body (in blue), C1R (in green), and their uncertainties (in red). Ellipses were fitted to C1R points, the black line stands for the best-fitted ellipse, and in gray is all the ellipses in the 1-sigma region. The left panel (a) is the event on 2017-06-22 and in the right panel (b) the event on 2017-07-23. For the sake of clarity, some redundant chords on 2017-07-23 were not plotted.

Table 2. Ring pole orientation (ICRS) obtained from events with multi-chords detections of CR1 and their 1σ uncertainties. Where r_{C1R}, P and B stands for the C1R radius, the position angle of the pole and the ring opening angle, respectively.

Parameter	2013-06-03[a]	2017-06-22	2017-07-23
r_{C1R} (km)	390.6 (03.3)	386.6 (12.3)	385.9 (00.4)
P (°)	-61.54 (0.10)	-62.13 (3.46)	-60.85 (0.11)
B (°)	+33.77 (0.41)	+52.33 (1.97)	+49.91 (0.11)
α_p (°)	151.25 (0.50)	149.46 (2.60)	151.03 (0.14)
δ_p (°)	+41.48 (0.22)	+40.98 (2.12)	+41.81 (0.07)
n.° det.	14	12	23[b]
χ^2_{pdf}	1.48	1.88	2.55

[a] Values from Braga-Ribas et al. (2014)
[b] The grazing chords were not used in the fit.

The results of Table 2 show a ~1σ consistency with the discovery results of 2013-06-03. Moreover, the values from 2017-07-23 are more accurate than previously published by Braga-Ribas et al. (2014). The invariance of the derived pole orienta-

tion of C1R over time indicates that no significant eccentricity is detected for that ring. This is discussed more quantitatively later.

4.2. C1 Ring structure

4.2.1. Radial profiles and eccentricity constraints

The high resolution data sets presented here allow the study of the fine structure of C1R. The event of 2017-04-09, observed from Namibia, was special for this purpose. In this event, we had five detections of C1R, as this is unsuitable for fitting all the ellipse's parameters, we fixed the pole orientation as obtained at 2017-07-23 to determine the centre position (f_0, g_0). With the fitted centre, it was possible to project the chords in the sky-plane to the rings' plane.

The untypical low velocity of the 2017-04-09 occultation (~5 km/s) allowed to probe Chariklo's ring with a resolution (Δr) of ~0.5 km per data point for the observations made at Wabi Lodge, Weaver Rocks Lodge, and Hakos. In this event, clear W-shaped structures appear in the different observations, see Figure 3 for more details.

From the occultation of 2017-07-23, the data sets from Danish telescope (Visual and Red filters) and from OPD allowed clear detection of similar W-shaped structures within C1R, see Figure 4 for details. The occultation's radial velocity at these stations allowed to probe Chariklo's ring with a resolution (Δr) of ~1.0 km in the ring-plane per data point. The VLT telescope had Δr on C1R of 2.2 km (exposure time of 0.1 seconds), so no clear structures were detected.

Using the resolved C1R profiles, we derive a mean radial width of ~6.9 km, with extreme values varying between ~4.8 and ~9.1 km for C1R, see Figure 5.

For order of magnitude estimation, we may assume that part of the width variation is associated with a $m = 1$ mode, in which case $W_r \sim [1 - q_e \cos(f)]\delta a$, with $q_e = e + a\partial e/\partial a$, where δe and δa are the variations of eccentricity (e) and semi-major axis (a) across the ring. By analogy with Uranus and Saturn's eccentric ringlets, we may assume that $a\partial e/\partial a \gg e$ (French et al. 1986). Adopting $\Delta W_r = 3.9$ km and $a = r_{C1R} = 385.6$ km, we obtain $\delta e \sim \delta W_r/2a \approx 0.005$. Relying again on Uranus and Saturn analogues, we expect e to be a few times δe, i.e. of the order of 0.01-0.02. This corresponds to full radial excursions of some ~10 km for the C1R ring. This is an easily detectable quantity, but with the difficulty that Chariklo's centre of mass must be pinned down at better than that distance. Those numbers are model dependent and should be taken with caution.

4.2.2. Two-band resolved profiles of C1R

The 2017-07-23 event was observed at the 1.54 meters Danish telescope at La Silla, using a dual system with a visible band (0.45-0.65 μm) and a red band (0.70-1.00 μm), see Skottfelt et al. (2015). Figure 6 displays the C1R and C2R radial profiles at immersion and emersion in both bands.

A visual inspection of Figure 6 clearly reveals the W-shaped structure of the C1R radial profiles. No significant differences between the two bands appear, as confirmed by the fitted parameters of the rings (see Tables C.1, C.1 and C.2), where no significant differences are noted at 1σ level.

The similarity of the radial profiles of C1R in the two bands indicates that this ring contains mostly particles larger than a few microns (Elliot et al. 1984). This is expected by analogy with the dense and narrow Saturnian or Uranian rings. In fact, the local Keplerian shear of the velocity field inside Chariklo's rings is

similar to that encountered in Saturn's or Uranus' rings (Sicardy et al. 2018). Moreover, water ice seems to be a major component of Chariklo's main ring (Duffard et al. 2014), as it is the case for Saturn's (and probably Uranus') rings. Thus, comparable collisional processes as those found in Saturn's or Uranus' rings are expected in C1R, and consequently comparable particle size distributions. In particular, the opacities of the dense Saturn's and Uranus' rings are dominated by cm- to meter-sized particles, with a very small amount of dust for both Saturn's (Cuzzi et al. 2018) and Uranus' (Esposito et al. 1991) rings, which are in line with our finding for C1R.

4.3. C2 Ring structure

Chariklo's C2R is narrower than C1R, with an orbital radius that was previously estimated to 405 km and an equivalent width that can vary between 0.1 and 1 km (Braga-Ribas et al. 2014; Bérard et al. 2017). This small size makes it very difficult to detect this ring. In this work we present unresolved detections, but most of the previous observations did not detect it. We obtained, here, the first multi-chord detection of C2R during the 2017-07-23 occultation.

As there is no resolved detection of C2R in this work, only the mid-times of each detection could be obtained. The ring radial width and opacity have large uncertainties and are highly correlated. A better defined quantity is then the equivalent width, for which we obtain a mean value 0.117 ± 0.08 km from the values listed in Table C.2, all obtained during the 2017-07-23 event.

Using the same approach described in sections 4.1 and 4.2.1, we fitted the best ellipse to obtain the global orbital parameters of C2R and compared the resulting centre, position angle and pole with those obtained for C1R during the same event. Figure 7 (panel (a)) displays the C2R chords and the corresponding best-fitted ellipse. A close-in view showing the fitted centres of C1R and C2R in the sky plane (panel (b)) reveals an offset of 2.28 km between those two centres at the ~3σ level. The radial offset Δr between C2R and C1R in the ring plane vs. the longitude, deduced from the respective elliptical fits, is displayed in panel (c). The grey area contains the 1σ uncertainty region for Δr, considering the respective uncertainties on the C1R and C2R fits.

Table 3 provides the fitted parameters obtained independently for C1R and C2R. We find that the two ring pole orientations are mutually consistent at a 1σ level. The 2.28-km offset between the rings centres might be indicative of a differential eccentricity of the order of $2.28/386 \sim 0.006$ between the two rings. However, we estimate that this 3σ level detection remains marginally significant. Finally, we find an average radial distance ΔR between C1R and C2R of 14 km, with a 1σ uncertainty interval of ~ 10-19 km which is in agreement with the mean value of 14.8 km found by Bérard et al. (2017).

Considering the multi-band detection of C2R with the Danish telescope, similar to the findings for C1R, no significant differences between the two filters appear, but due to its poorer detection level, differences can be hidden within the noise.

4.4. Search for faint ring material between C1R and C2R

Our best light curves in terms of time resolution and SNR were obtained during the 2017-07-23 event at VLT, OPD, and Danish telescope (La Silla). They can be used to detect or place an upper limit of material orbiting in the gap between C1R and C2R. We
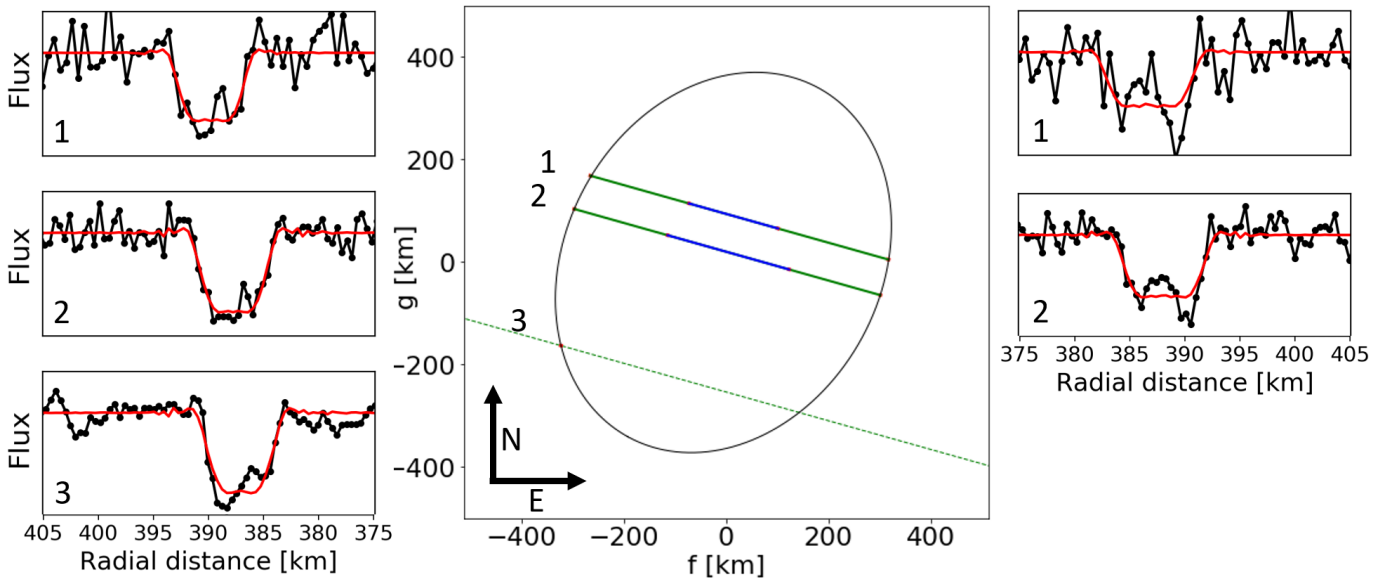
Fig. 3. Results of the 2017-04-09 event. The central plot displays the occultation chords projected in the sky-plane for the main body (in blue), C1R (in green), and their uncertainties (red segments). The black line is the best-fitting ellipse to the C1R point, considering a fixed pole orientation (as determined in Section 4.1). The side panels display the normalised radial ring profiles, projected in the ring-plane, numbered as follows: Wabi Lodge (1), Weaver Rocks Lodge (2), and Hakos (3), the right panels contain the first detection (immersion) at each station and the left panels contain the seconds detections (emersion). As mentioned in Appendix A and shown in Appendix F, the Hakos light curve contains only the emersion detection of the ring due to bad weather conditions at immersion. We call attention to the unambiguous detection of W-shaped structures within the C1R.

Table 3. Parameters obtained on 2017-07-23 from fitting ellipses over C1R and C2R projections in the sky-plane.

Parameter	C1R	C2R
f_0 (km)	-22.0 (0.1)	-22.5 (0.2)
g_0 (km)	-04.8 (0.1)	-07.1 (0.4)
r (km)	385.9 (0.4)	399.8 (0.6)
P (°)	-60.85 (0.11)	-61.18 (0.19)
B (°)	+49.91 (0.11)	+49.99 (0.16)
α_p (°)	151.03 (0.14)	150.91 (0.22)
δ_p (°)	+41.81 (0.07)	+41.60 (0.12)
n.° det.	23	08
χ^2_{pdf}	2.55	0.68

assume that this putative semi-transparent material is concentric and co-planar to C1R and C2R.

Following similar procedures as described in Bérard et al. (2017), we convert each data-point (i) from flux to equivalent width (E_p) using Equation (6), where $\phi(i)$ is the normalised light-flux, and $\Delta r(i)$ is the radial resolution in the ring plane travelled by the star during one exposure ($\Delta t(i)$),

$$E_p(i) = \frac{|\sin(B)|}{2} \cdot [1 - \phi(i)] \cdot \Delta r(i) . \quad (6)$$

The top panel (a) of Figure 8 contains a plot of $E_p(i)$ over the radial distance in the ring plane $R(i)$ for the observation at OPD. The 1-sigma limit for the equivalent width ($E_p(1\sigma)$) for the region between C1R and C2R in the ring plane (between 391 and 399 km) was of 24 meters, this means that if there were an uninterrupted ring between C1R and C2R with normal opacity greater than (p_n) of 0.003 (0.009) it would have been detected

with a 1-sigma (3-sigma) confidence level. As for the VLT observation with a Δr of 2.2 km, it only contains three data points between C1R and C2R for each detection. For this data-set a ring with normal opacity of 0.011 would have been detected within 3-sigma confidence level, as can be seen in the mid panel (b) in Figure 8.

Another approach is the combination of some data to increase the quality of the measurement. As shown in Section 4.2.2, the Danish observations in two different filters are virtually the same (within the errors), meaning that these two observations can be combined to improve the quality of the data. Using the combination of both light curves illustrated in the bottom panel (c) in Figure 8 we obtain an $E_p(1\sigma)$ of 16 meters. A ring material between C1R and C2R with normal opacity greater than 0.002 (0.006) would have been detected with at 1-sigma (3-sigma) confidence level.

## 5. Chariklo's size, shape and rotational parameters

Between 2013 and 2020, Chariklo was the target of several successful stellar occultations. That allows us to go further than only the determination of its apparent size and shape. It enables us to determine Chariklo's 3D shape. We can also analyse the centre position of Chariklo and how it compares with its rings' centre, thus giving us constraints on Chariklo rings' excentricity. Finally, we can evaluate Chariklo's rotational parameters (rotational light curve amplitude) to see how our model compares with previous observations.

5.1. Chariklo's 3D shape

First, let us consider that Chariklo's pole orientation is the same as its rings and, as we show in Section 4.1, C1R pole orientation can be considered fixed between 2013 and 2017.
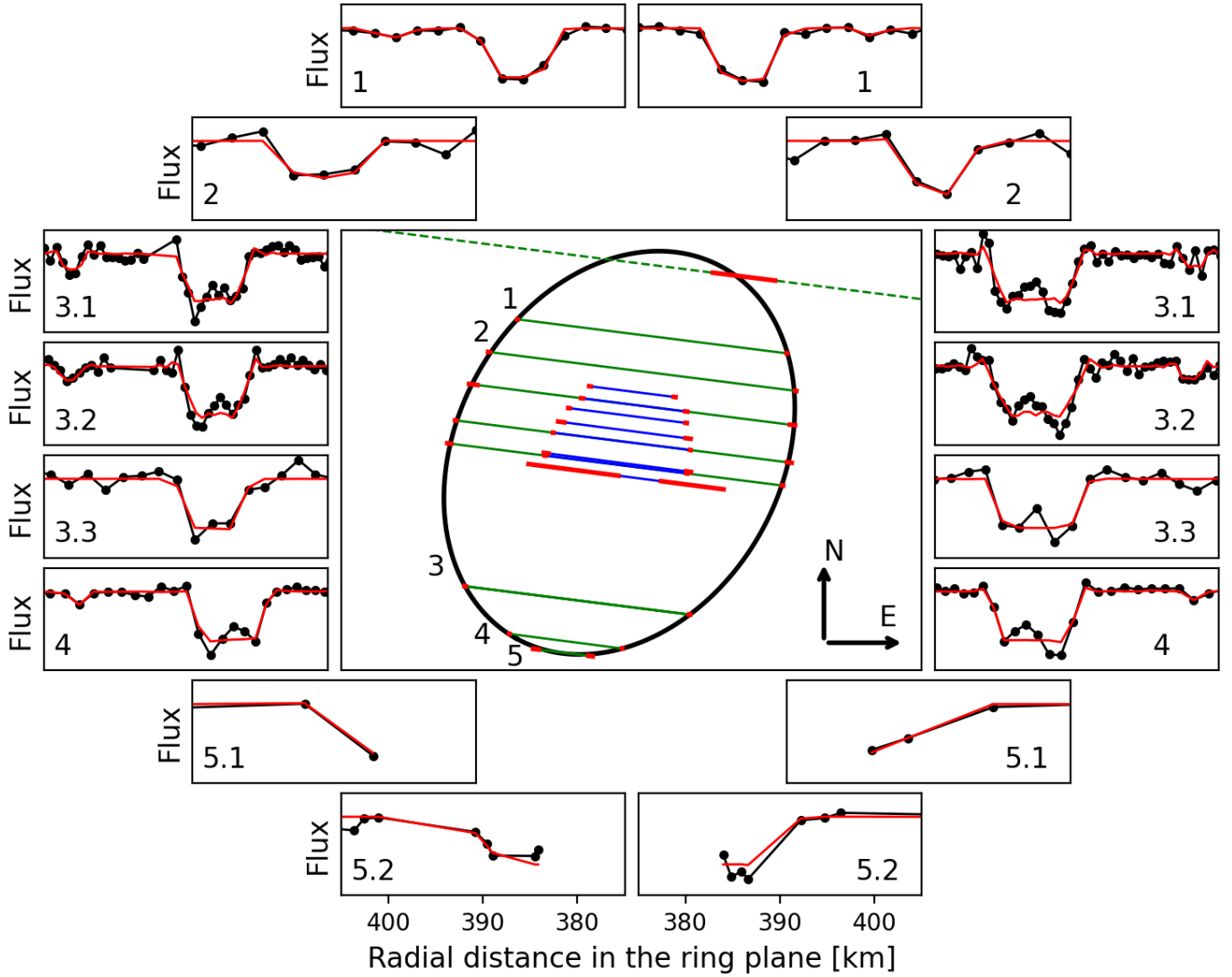
Fig. 4. Same as Figure 3 for the 2017-07-23 event. The side panels are numbered as follows: Cerro Paranal (1), Tolar Grande (2), La Silla (3), Observatório Pico dos Dias (4) and Cerro Tololo (5). The observations on La Silla were made using the Danish telescope dual experiment in the Visual (3.1) and Red bands (3.2) and a 1-meter telescope (3.3). The left panels contain the first detection (immersion) at each station and the right panels contain the seconds detections (emersion). The observations on Cerro Tololo were grazing over C1R and they were made using the SARA (5.1) and PROMPT (5.2). For sake of clarity, some redundant chords were visually suppressed.
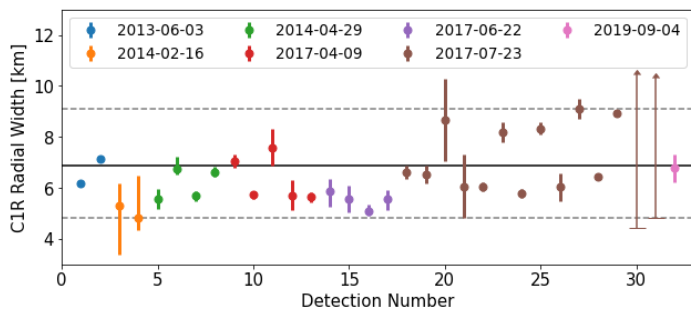
Fig. 5. C1R radial width for all the obtained resolved detections. Note that the PROMPT and SARA values only provide lower limits to the radial width. The black line represents the mean value of W_r (6.9 km) with the gray dashed line as the minimum and maximum values (4.8 and 9.1 km).

As an initial guess, we will consider that the centre of Chariklo and its rings are the same. This assumption will allow

us to consider 11 stellar occultations that had at least one chord over Chariklo's main body and at least two ring detections. The only exception was the occultation on 2019-08-08 that had five detections of the main body, but no ring detection. In Section 5.3 we will further analyse Chariklo's centre and use it to derive an upper limit to Chariklo's rings excentricities.

We also consider that Chariklo's rotational period is known and equals 7.004 ± 0.036 (Fornasier et al. 2014). Even though we know Chariklo's period, the period uncertainty is large enough that its rotational phase cannot be determined at the moment of each occultation. In other words, it can be any value between 0 and 360 degrees.

Our analysis considers the rotational elements as described in Archinal et al. (2018). The angle $W(t)$ specifies the position of the prime meridian (in this work chosen to be in the direction of the longest axis) on a given date (considering light time between Chariklo and the observer), W_0 is the value of W at the reference epoch (t_{ref}) and $\dot{W}$ stands for the rotation rate, here expressed in
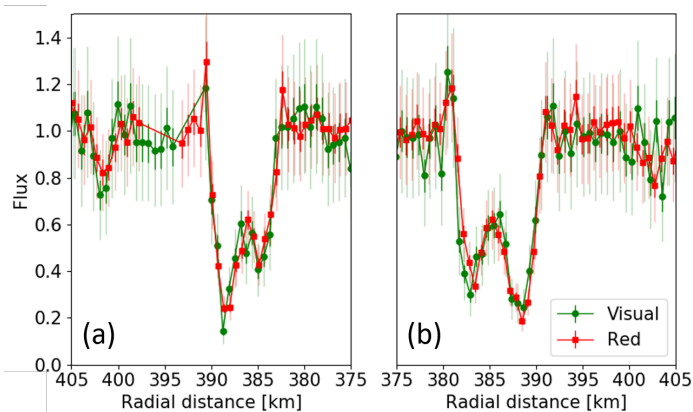
Fig. 6. The normalised radial profiles of C1R and C2R projected in the ring plane, as observed from the 1.54-m Danish telescope during the 2017-07-23 event. Green points: the visual channel (0.45-0.65 μm); red points: the red channel (0.70-1.0 μm). The darker (resp. lighter) error bars are for the 1σ (resp. 3σ) level stemming from the SNR of the target source and the calibrators. The (a) and (b) panels stands for the first detection (immersion) and the second detection (emersion), respectively. We call attention to the agreement between the visual and the red channels in both detections.

Fig. 8. Equivalent width of ring material over the radial distance in the ring plane for the observations in OPD/LNA (a), VLT/ESO (b) and Danish/ESO (c). We determine a 3-sigma upper limit of semi-transparent uninterrupted material between C1R and C2R with normal opacity of 0.006.

Fig. 7. Panel (a): the occultation chords of the 2017-07-23 event detected, for Chariklo's main body (blue) and for the C2R ring (cyan). The uncertainties at the extremities of the chords are indicated in red. For sake of clarity, the C1R chords are not reproduced here, and can be seen in Figures 2 and 4. The fitted ellipses to the C2R is drawn in black. The 1σ uncertainty region of that fit is indistinguishable from the black line thickness at this scale. The best fitted ellipse to the C1R ring detections is shown in green. Panel (b): the fitted centres of C1R (green) and C2R (black) in the sky plane. The darker colours stands for the simultaneous 1σ uncertainty regions (corresponding to the $\chi^2_{min} + 2.3$ criterion), while the lighter colours stands for the 3σ regions ($\chi^2_{min} + 11.4$ criterion). The red dashed line shows a 2.28-km offset between the C1R and C2R centres. Panel (c): the radial difference Δr (in the ring-plane) between C2R and C1R vs. the longitude, deduced from the elliptical fits of panel (a). The grey zone delimits the 1σ region associated with the uncertainties on C1R and C2R. It shows that at that level, no significant radial distance variations between C1R and C2R are detected.

degrees per days,

$$W(t) = W_0 + \dot{W}(t - t_{ref}) . \tag{7}$$

The reference epoch was chosen as the time of the first stellar occultation considered here, 2013-06-03 06:25:00 UTC (2456446.767361111 JD), to minimise error propagation. Let us consider a given 3D ellipsoidal model with semi-axis $a > b > c$,

rotating around its smallest axis (c). We project this ellipsoid in the sky-plane and determine its projected limb as the points where gradient of the normal to the direction to the observer is equal to zero.

The model limb is then compared with the occultations chords, and chi-squared statistics are computed using

$$\chi^2 = \sum_i^N \frac{(r_i - r'_i)^2}{\sigma_i^2 + \sigma_{model}^2}, \tag{8}$$

where r_i is the radial distance of the ith observed chord extremity, r'_i is the radial distance of the ellipsoid limb, σ_i is the observed radial uncertainty of each extremity point and σ_{model} consist of the uncertainty of our ellipsoidal model in contrast with Chariklo's real 3D shape, for instance the existence of topographic features within Chariklo's surface. σ_{model} was estimated iteratively as 3 km, so the resulting χ^2 per degree of freedom would be close to 1.

We compute this for 10,000,000 models, varying a, b, c, W_0 and $\dot{W}$. As we do not intend to fit the rotation rate, we let it vary between 1227.20 and 1239.95 deg/days only. This value was obtained considering a period between 6.968 and 7.040 hours, as provided by Fornasier et al. (2014). For the other parameters, we let a, b, c vary in the range of 125 ± 50 km and W_0 between 0 and 360 degrees.

Our best fitted value was the ellipsoid with semi-axis equals to $143.8^{+1.4}_{-1.5}$, $135.2^{+1.4}_{-2.8}$ and $99.1^{+5.4}_{-2.7}$ km with χ^2_{pdf} equal to 0.688. Figure 9 shows this ellipsoid fitted to the observational data. The standard deviation of the radial residuals was 4.11 km (2.8% considering a volume equivalent radius of 124.8 km), with a maximum value of 7.78 km and a minimum of -5.52 km, this can indicate topographic features of this range on Chariklo's surface.

5.2. Chariklo's density

After fitting an ellipsoid to Chariklo, the first thing that becomes clear is that Chariklo does not have a shape corresponding with the equilibrium figure of a Maclaurin spheroid (where a would be equal to b). Instead, if we consider the Jacobi figure, the ex-
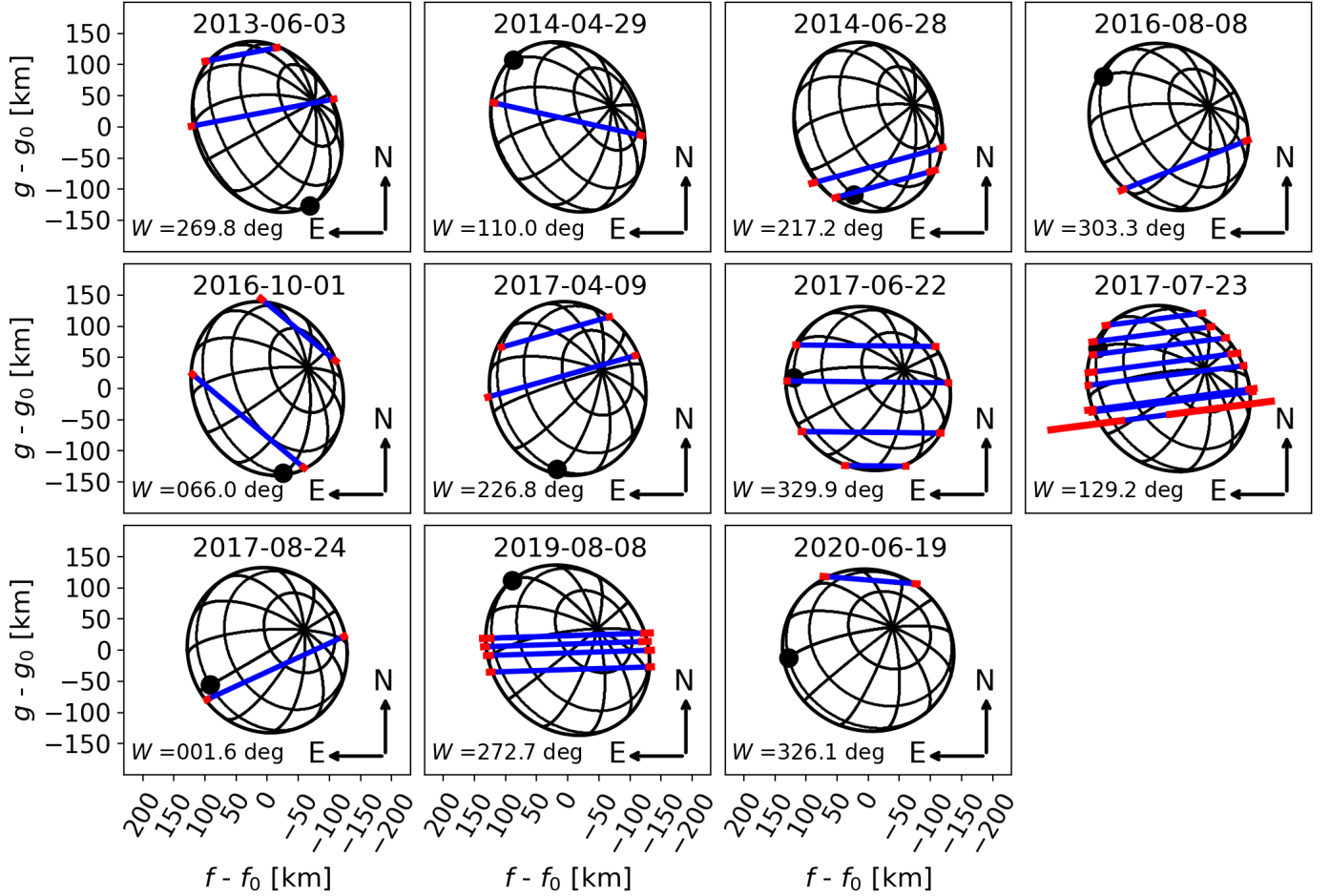
Fig. 9. Ellipsoidal model that best fits the 11 stellar occultations observed between 2013-06-23 and 2020-06-19. Each panel corresponds to an occultation event identified by the time stamp in the upper part of each one. The blue lines stands for the observed chords with their uncertainties in red. The black dot indicates the intersection between the equator and the prime meridian, which is used as the reference to define the rotation angle W, written in the lower left of each panel.

pected uniform density (ρ) of Chariklo would be $1.55^{+0.05}_{-0.08}\ g/cm^3$, as can be calculated with Equation (9),

$$\Omega = \frac{2\pi}{G\rho T^2} = \beta\gamma \int_0^\infty \frac{u}{(1+u)(\beta^2+u)\Delta(u,\beta,\gamma)}du\,, \quad (9)$$

$$\Delta(u,\beta,\gamma) = \sqrt{(1+u)(\beta^2+u)(\gamma^2+u)}\,, \quad (10)$$

where G is the gravitational constant, T is the rotational period, β and γ stand for the semi-axis ratios b/a and c/a respectively, more details in Sicardy et al. (2011), Ortiz et al. (2017) and references therein. This density is not consistent with the expected value, between 0.79 and 1.04 g/cm^3, of a body with a rotational period (T) of 7.004 hours. For a stable Jacobi ellipsoid, the shapes should lie with the dimensionless parameter Ω between 0.284 and 0.374 (Tancredi & Favre 2008), instead of 0.191 as obtained in our analysis.

On the other hand, one possibility is that Chariklo rings' particles would be close to the 1/3 resonance with the central body Sicardy et al. (2019). That means that the particles complete one revolution while the body completes three rotations. In this context, an ellipsoid with a semi-axis of 143.8, 135.2 and 99.1 km should have a density between 0.73 and 0.85 g/cm^3, so the 1/3 resonance would be between 385 and 405 km, the region where the Chariklo rings' particles are. These are indications that the

hydrostatic equilibrium of a homogeneous body does not dominate Chariklo's shape.

5.3. Comparing Chariklo's centre with its rings' centre

As mentioned in Section 5.1, we considered that Chariklo's centre is the same as its rings' centre. Any deviation from this would appear as a systematic effect unique to each stellar occultation. In extreme cases (tens of kilometres), this would also preclude a unique solution with the methodology applied. That is not the case, as can be seen from Figure 9.

We used our derived 3D model and fitted it for the centre on the chords of 2017-07-23 multi-chord detection, to check for small systematic effects. Here we compare the fitted value for Chariklo main body and the centre obtained for its rings (values in Table 3). We obtain a radial difference between the main body and C1R of $2.46^{+2.86}_{-2.07}$ km in the sky plane considering an 1-sigma confidence level. At a 3-sigma level, this value is between zero and 8.41 km. If we consider that this offset is in the ring plane, this could be translated to a $2.51^{+2.84}_{-2.50}$ km difference, in a 3-sigma confidence level ranging between 0 and 8.55 km.

The 1-sigma (3-sigma) region's limit can give us hints about the maximum difference between Chariklo's centre and the centre of its rings. This value cannot be larger than 5.35 (8.55) km at the moment of the detected occultations. These values give us

an upper limit of the eccentricity of C1R rings of about 0.014 (0.022).

Applying the same analysis to C2R as observed on 2017-07-23, we obtain a maximum radial distance of 3.27 (6.84) km in the ring plane. This is representing an upper limit of about 0.0082 (0.0171) for C2R eccentricity considering a 1-sigma (3-sigma) confidence level.

5.4. Rotational light curve amplitude

Considering Chariklo's rotational light curve, we can check if our ellipsoidal model can explain the light curve amplitude provided by Leiva et al. (2017) as observed by Davies et al. (1998); Peixinho et al. (2001); Galiazzo et al. (2016); Fornasier et al. (2014); Leiva et al. (2017), and listed in Table 4.

Table 4. Rotational light curve amplitudes from the literature. The alias column is a simplified reference name, the first letter of the main author's name, plus the two last digits of publication year.

Date	Δmag	Reference	Alias
1997-05	< 0.02	Davies et al. (1998)	D98
1999-03	< 0.05	Peixinho et al. (2001)	P01
2006-06	0.13 ± 0.03	Galiazzo et al. (2016)	G16
2013-06	0.11 ± 0.02	Fornasier et al. (2014)	F14
2015-07	0.06 ± 0.02	Leiva et al. (2017)	L17

We calculate the magnitude amplitude using Equation (11) as derived by Fernández-Valenzuela et al. (2017) and references therein,

$$\Delta m = -2.5 \, log \frac{A_{min}p_V + A_r(I/F)}{A_{max}p_V + A_r(I/F)} \, , \qquad (11)$$

where A_{min} and A_{max} stands for the smallest/largest covered area by the 3D model, A_r is the area covered by Chariklo's rings. Here we consider Chariklo's geometric albedo (p_V) as 3.7% and the ring reflectivity (I/F) as 4.9% (Leiva et al. 2017). As shown in Figure 10 our 3D model can explain the observed light curve amplitude. Any slight difference can be associated with albedo variegation.
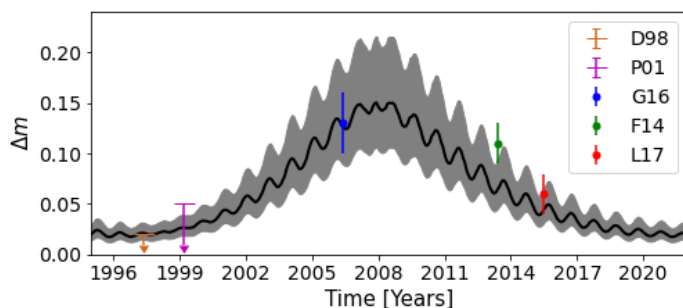
Fig. 10. Rotational light curve's amplitude variations over the years. In black is our best fitted ellipsoidal model, and in grey all the ellipsoids within the 1-sigma region. We compare our model with the observation detailed in Table 4.

6. Astrometric positions

A valuable by-product of stellar occultations is the mas-level precision of the occulting body astrometry, especially since the Gaia DR2 and EDR3 catalogues provide the stars' positions at sub-mas-level precision (Desmars et al. 2019; Herald et al. 2020; Rommel et al. 2020). This means a significant improvement of the occulting body ephemerides, which in turn allows better predictions for future events in a virtuous loop.

We obtained Chariklo's astrometric positions from seven stellar occultations observed between 2017 and 2020, assuming that the centre of Chariklo coincides with the centre of C1R. Note that the 2019-09-04 occultation only gives the egress detection of C1R, so that no astrometric constraints can be derived from that event, more details in Appendix E. Table 5 lists the positions obtained and their associated uncertainties. Those uncertainties stem from the uncertainties of the fitted ring centre (σf_0, σg_0) and the uncertainties in the star positions propagated to the occultation epoch (see Table 1). Note that the resulting uncertainties are usually at sub-mas level, corresponding to a few kilometres at Chariklo's distance, where 1 mas ~10 km.

Those positions were used to improve Chariklo's ephemeris using the NIMA software (Desmars et al. 2015). The corresponding bsp file (NIMA v.19) can be downloaded from the Lucky Star website[7]. The updated ephemeris provides a propagated uncertainty on Chariklo's position of 2 mas in right ascension and declination, as of January 2022. This corresponds to roughly 20 km at Chariklo's distance.

7. Conclusions

This paper presents results from eight unpublished stellar occultations by Chariklo and its rings, observed between 2017 and 2020. Our main results are:

(i) For the first time, we detected stellar occultations with three (or more) chords over Chariklo's main body;

(ii) We obtained the second and third multi-chord detections of C1R since Chariklo's rings discovery (2013-06-03);

(iii) For the first time, we obtained multi-chord detections of C2R;

(iv) We obtained the first simultaneous multi-band observation of Chariklo's rings;

(v) New astrometric data for the Chariklo system was obtained from all the detected stellar occultations, including two single-chord and one double-chord events.

Table 6 contains a summary of our main results. We determined a Chariklo's rings pole orientation consistent with, and more precise than those previously determined by Braga-Ribas et al. (2014). We could not refute Chariklo's ring to be circular within our measurements' errors. We estimate an upper 3σ limit of 0.022 for the eccentricity of C1R. By analogy with Uranus' and Saturn's ringlets, and from its width variations, we estimate an eccentricity greater than ~0.005 for that ring which remains, however, model dependent.

The observation on 2017-04-09 and some of 2017-07-23 allowed to probe C1R with a radial resolution of ~0.5 and ~1.0 km, respectively. This high resolution allowed precise detection of W-shaped structures within C1R. Also, there is a clear difference between the structures over the detections, as shown in Figure 11 containing all resolved detections since 2014. From our observations, we detect that the mean radial width of C1R is ~6.9 km and can range between ~4.8 and ~9.1 km.

---

[7] https://lesia.obspm.fr/lucky-star/obj.php?p=624

Table 5. Astrometric Chariklo's positions for each event.

Date and time UTC	Right Ascension[a]	Declination[a]
2020-06-19 15:51:00.000	$20^h\ 02^m\ 32^s.0002322 \pm 0.339$ mas	-22° 20' 41".488487 ± 0.227 mas
2019-08-08 21:41:00.000	$19^h\ 31^m\ 49^s.7910264 \pm 0.227$ mas	-25° 34' 26".785014 ± 0.544 mas
2019-08-02 10:02:00.000	$19^h\ 33^m\ 07^s.4812764 \pm 0.872$ mas	-25° 34' 42".519146 ± 1.187 mas
2017-08-24 02:59:00.000	$18^h\ 42^m\ 35^s.2371826 \pm 0.426$ mas	-31° 09' 50".561462 ± 0.432 mas
2017-07-23 05:58:00.000	$18^h\ 48^m\ 09^s.2288885 \pm 0.103$ mas	-31° 26' 32".437598 ± 0.096 mas
2017-06-22 21:18:00.000	$18^h\ 55^m\ 15^s.6602082 \pm 0.116$ mas	-31° 31' 21".621802 ± 0.110 mas
2017-04-09 02:24:00.000	$19^h\ 04^m\ 03^s.6255610 \pm 0.129$ mas	-31° 17' 15".257638 ± 0.127 mas

[a] The positions assume the EDR3 star positions given in Table 1

Table 6. Summary of the obtained parameters for Chariklo and its rings.

	Parameter	Value	Comments
	Radius	385.9 ± 0.4 km	See Section 4.1
	Pole orientation (RA)	151.03 ± 0.14 deg	See Section 4.1
	Pole orientation (Dec)	+41.81 ± 0.07 deg	See Section 4.1
C1 Ring	Mean width	6.86 km	See Section 4.2.1
	Width variation	$4.8 \leq W_r \leq 9.1$ km	See Section 4.2.1
	Eccentricity	$0.005 \leq e_{C1R} \leq 0.022$	See Section 4.2.1 and 5.3
	Particle's size	> 1.0 micron	See Section 4.2.2
Gap between	Radial distance between rings	$13.9^{+5.2}_{-3.4}$ km	See Section 4.3
C1R and C2R	Equivalent width of material in gap	< 0.048 km	See Section 4.4
	Radius	399.8 ± 0.6 km	See Section 4.3
	Pole orientation (RA)	150.91 ± 0.22 deg	See Section 4.3
C2 Ring	Pole orientation (Dec)	+41.60 ± 0.12 deg	See Section 4.3
	Equivalent width	0.117 ± 0.080 km	See Section 4.3
	Eccentricity	< 0.017	See Section 5.3
	a (Semi-major axis)	$143.8^{+1.4}_{-1.5}$ km	See Section 5.1
Chariklo	b (Semi-median axis)	$135.2^{+1.4}_{-2.8}$ km	See Section 5.1
	c (Semi-minor axis)	$99.1^{+5.4}_{-2.7}$ km	See Section 5.1
	Volume equiv. radius	$124.8^{+3.0}_{-2.3}$ km	See Section 5.1

The Danish 1.54 meters telescope in La Silla observed the event on 2017-07-23 in two different bands, visual (0.45-0.65 microns) and red (0.70-1.00 microns). There is no significant difference between these two observations, what can be interpreted as that Chariklo's ring is mostly made by particles larger than a few microns.

The observations from the large telescope's facilities on 2017-07-23 allowed for the first time a multi-chord detection of C2R. From this, we can do an independent analysis of C2R and C1R and compare the obtained values. We obtained a 1-sigma agreement between the rings' pole orientation, a strong argument that they are coplanar, as expected. There is a slight difference between the centre position of both rings. That can be explained as a differential eccentricity between both rings, but this is not significant at the 3-sigma level. The determined radial difference in the ring plane between C1R and C2R is 14^{+7}_{-8} km. We checked

for material between C1R and C2R and determined a 3-sigma upper limit of a ring material with normal opacity of 0.006.

Multiple stellar occultations between 2013 and 2020 combined with statistical analysis allowed the determination of Chariklo's 3D size and shape. We fitted 11 stellar occultations and determined that Chariklo is consistent with a triaxial ellipsoid with semi-axes of $143.8^{+1.4}_{-1.5}$, $135.2^{+1.4}_{-2.8}$ and $99.1^{+5.4}_{-2.7}$, and a volume equivalent radius of $124.8^{+3.0}_{-2.3}$. These values are consistent, within error bars, with previous values derived from occultations (Leiva et al. 2017). We highlight that the new data, including multi-chord occultations, reduced the uncertainty of the modelled parameters. This 3D-shape is essential for constraining the dynamics of Chariklo's ring system.

Stellar occultations provide Chariklo's astrometric positions at mas-precision level, even for single- or double-chords observations. Those positions have been implemented in the NIMA software to update Chariklo's ephemeris. It has a propagated uncer-
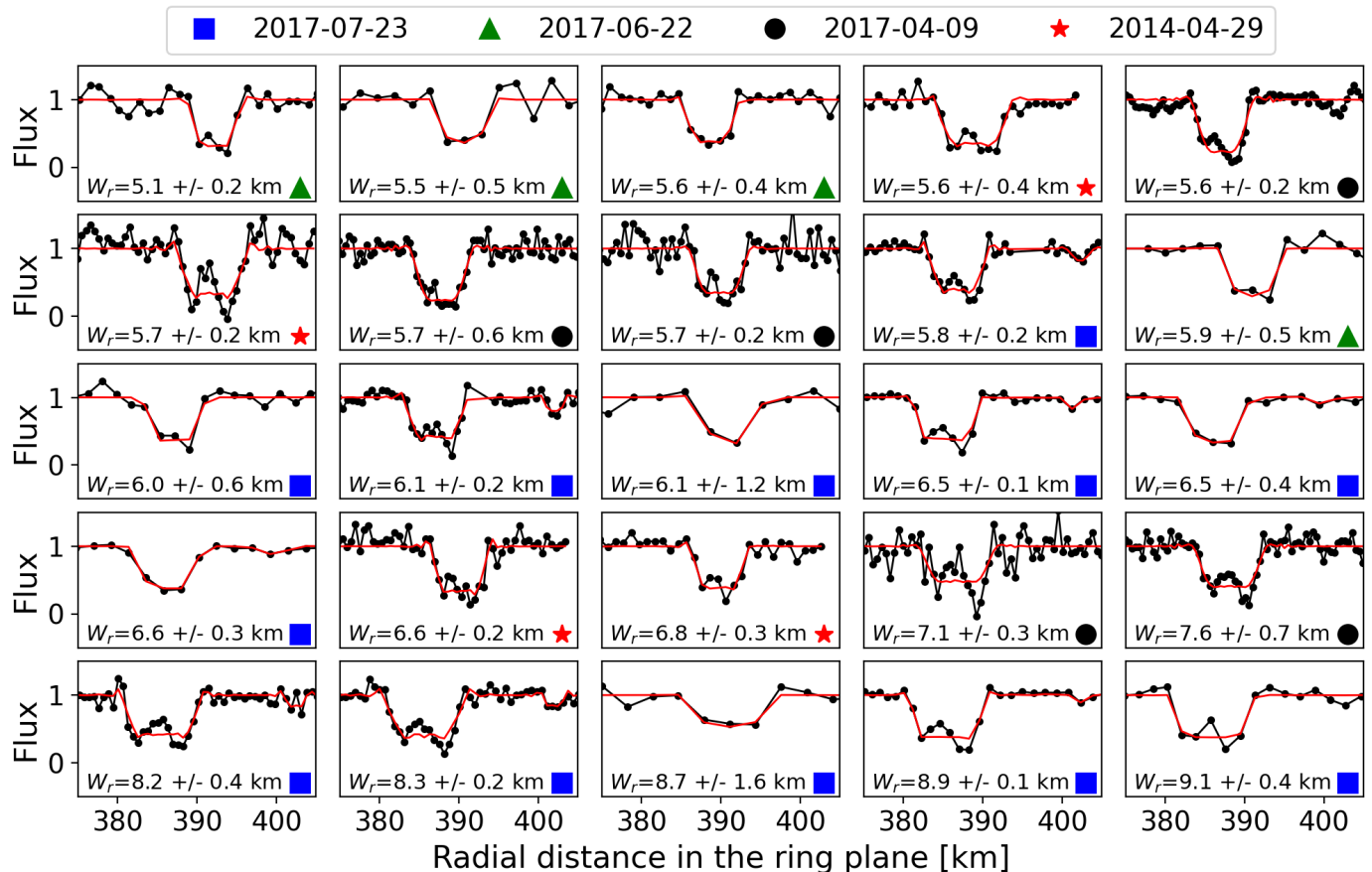
Fig. 11. All resolved detections of Chariklo C1R over radial distance in the ring plane. The black dots represents the observed flux and the red line is the best fitted model. The detections were sorted by radial width, as written in the lower part of each panel. The symbols in the lower right of each panel represents the different occultations. The data and analysis of the 2014-04-29 occultation was obtained from Bérard et al. (2017).

tainty of ∼5 mas (∼50 km at Chariklo's distance) up to January 2022. The 50-km uncertainty is small compared to Chariklo's diameter (∼260 km) and the ring span (∼800 km). This permits a careful planning of future occultations with a high rate of success. In addition to Chariklo's, the ephemerides of other small bodies with comparable accuracies are available on the Lucky Star webpage[8].

The parameters obtained in this work should be useful for constraining dynamical models of Chariklo and its rings, and provide new insights into the formation and evolution of this system.

References

Altenhoff, W. J., Menten, K. M., & Bertoldi, F. 2001, A&A, 366, L9
Anderson, B. 2019, Journal for Occultation Astronomy, 9, 9
Araujo, R. A. N., Winter, O. C., & Sfair, R. 2018, MNRAS, 479, 4770
Archinal, B. A., Acton, C. H., A'Hearn, M. F., et al. 2018, Celestial Mechanics and Dynamical Astronomy, 130, 22
Assafin, M., Camargo, J. I. B., Vieira Martins, R., et al. 2012, A&A, 541, A142
Assafin, M., Vieira Martins, R., Camargo, J. I. B., et al. 2011, in Gaia follow-up network for the solar system objects : Gaia FUN-SSO workshop proceedings, 85–88
Astropy Collaboration, Robitaille, T. P., Tollerud, E. J., et al. 2013, A&A, 558, A33

Bauer, J. M., Grav, T., Blauvelt, E., et al. 2013, ApJ, 773, 22
Bérard, D., Sicardy, B., Camargo, J. I. B., et al. 2017, AJ, 154, 144
Braga-Ribas, F., Sicardy, B., Ortiz, J. L., et al. 2013, ApJ, 773, 26
Braga-Ribas, F., Sicardy, B., Ortiz, J. L., et al. 2014, Nature, 508, 72
Butcher, H. & Stevens, R. 1981, Kitt Peak National Observatory Newsletter, 16, 6
Butkevich, A. G. & Lindegren, L. 2014, A&A, 570, A62
Camargo, J. I. B., Vieira-Martins, R., Assafin, M., et al. 2014, A&A, 561, A37
Campins, H. & Fernández, Y. 2002, Earth Moon and Planets, 89, 117
Cuzzi, J. N., Filacchione, G., & Marouf, E. A. 2018, The Rings of Saturn, 51–92
Davies, J. K., McBride, N., Ellison, S. L., Green, S. F., & Ballantyne, D. R. 1998, Icarus, 134, 213
Desmars, J., Camargo, J., Berard, D., et al. 2017, in AAS/Division for Planetary Sciences Meeting Abstracts, Vol. 49, AAS/Division for Planetary Sciences Meeting Abstracts #49, 216.03
Desmars, J., Camargo, J. I. B., Braga-Ribas, F., et al. 2015, A&A, 584, A96
Desmars, J., Meza, E., Sicardy, B., et al. 2019, A&A, 625, A43
Duffard, R., Pinilla-Alonso, N., Ortiz, J. L., et al. 2014, A&A, 568, A79
Elliot, J. L., French, R. G., Meech, K. J., & Elias, J. H. 1984, AJ, 89, 1587
Esposito, L. W., Brahic, A., Burns, J. A., & Marouf, E. A. 1991, Particle properties and processes in Uranus' rings., ed. J. T. Bergstralh, E. D. Miner, & M. S. Matthews, 410–465
Fernández-Valenzuela, E., Ortiz, J. L., Duffard, R., Morales, N., & Santos-Sanz, P. 2017, MNRAS, 466, 4147
Fornasier, S., Lazzaro, D., Alvarez-Candal, A., et al. 2014, A&A, 568, L11
Fornasier, S., Lellouch, E., Müller, T., et al. 2013, A&A, 555, A15
French, R. G., Elliot, J. L., & Levine, S. E. 1986, Icarus, 67, 134
French, R. G., Nicholson, P. D., Porco, C. C., & Marouf, E. A. 1991, Dynamics and structure of the Uranian rings., ed. J. T. Bergstralh, E. D. Miner, & M. S. Matthews, 327–409
Gaia Collaboration, Brown, A. G. A., Vallenari, A., et al. 2018, A&A, 616, A1
Gaia Collaboration, Brown, A. G. A., Vallenari, A., et al. 2021, A&A, 649, A1
Gaia Collaboration, Brown, A. G. A., Vallenari, A., et al. 2016a, A&A, 595, A2
Gaia Collaboration, Prusti, T., de Bruijne, J. H. J., et al. 2016b, A&A, 595, A1
Galiazzo, M., de la Fuente Marcos, C., de la Fuente Marcos, R., et al. 2016, Ap&SS, 361, 212
Herald, D., Gault, D., Anderson, R., et al. 2020, MNRAS, 499, 4570
Hyodo, R., Charnoz, S., Genda, H., & Ohtsuki, K. 2016, Astrophys. J. Letters, 828, L8
Jewitt, D. & Kalas, P. 1998, ApJ, 499, L103
Leiva, R., Sicardy, B., Camargo, J. I. B., et al. 2017, AJ, 154, 159
Lellouch, E., Moreno, R., Müller, T., et al. 2017, A&A, 608, A45
Melita, M. D., Duffard, R., Ortiz, J. L., & Campo-Bagatin, A. 2017, A&A, 602, A27
Michikoshi, S. & Kokubo, E. 2017, ApJ, 837, L13
Nicholson, P. D., De Pater, I., French, R. G., & Showalter, M. R. 2018, The Rings of Uranus, ed. M. S. Tiscareno & C. D. Murray, 93–111
Ortiz, J. L., Duffard, R., Pinilla-Alonso, N., et al. 2015, A&A, 576, A18
Ortiz, J. L., Santos-Sanz, P., Sicardy, B., et al. 2017, Nature, 550, 219
Pan, M. & Wu, Y. 2016, ApJ, 821, 18
Pavlov, H. 2020, Tangra: Software for video photometry and astrometry
Peixinho, N., Lacerda, P., Ortiz, J. L., et al. 2001, A&A, 371, 753
Rommel, F. L., Braga-Ribas, F., Desmars, J., et al. 2020, A&A, 644, A40
Sekiguchi, T., Ootsubo, T., Hasegawa, S., et al. 2012, in Asteroids, Comets, Meteors 2012, Vol. 1667, 6477
Sicardy, B., Buie, M. W., Benedetti-Rossi, G., et al. 2015, in AAS/Division for Planetary Sciences Meeting Abstracts, Vol. 47, AAS/Division for Planetary Sciences Meeting Abstracts #47, 104.01
Sicardy, B., El Moutamid, M., Quillen, A. C., et al. 2018, Rings Beyond the Giant Planets, ed. M. S. Tiscareno & C. D. Murray, 135–154
Sicardy, B., Leiva, R., Renner, S., et al. 2019, Nature Astronomy, 3, 146
Sicardy, B., Ortiz, J. L., Assafin, M., et al. 2011, Nature, 478, 493
Sickafoose, A. A., Bosh, A. S., Emery, J. P., et al. 2020, MNRAS, 491, 3643
Skottfelt, J., Bramich, D. M., Hundertmark, M., et al. 2015, A&A, 574, A54
Souami, D., Braga-Ribas, F., Sicardy, B., et al. 2020, A&A, 643, A125
Tancredi, G. & Favre, S. 2008, Icarus, 195, 851
Ticha, J., Tichy, M., Moravec, Z., et al. 1997, Minor Planet Electronic Circulars, 1997-D11

[1] LESIA, Observatoire de Paris, Université PSL, CNRS, Sorbonne Université, Univ. Paris Diderot, Sorbonne Paris Cité, 5 place Jules Janssen, 92195 Meudon, France
e-mail: morgado.fis@gmail.com

[2] Laboratório Interinstitucional de e-Astronomia - LIneA, Rua Gal. José Cristino 77, Rio de Janeiro, RJ 20921-400, Brazil
[3] Observatório Nacional/MCTI, R. General José Cristino 77, CEP 20921-400 Rio de Janeiro - RJ, Brazil
[4] Federal University of Technology - Paraná (UTFPR / DAFIS), Rua Sete de Setembro, 3165, CEP 80230-901, Curitiba, PR, Brazil
[5] Institut Polytechnique des Sciences Avancées IPSA, 63 boulevard de Brandebourg, 94200 Ivry-sur-Seine, France
[6] Institut de Mécanique Céleste et de Calcul des Éphémérides, IMCCE, Observatoire de Paris, PSL Research University, CNRS,Sorbonne Universités, UPMC Univ Paris 06, Univ. Lille, 77, Av. Denfert-Rochereau, 75014 Paris, France
[7] UNESP - São Paulo State University, Grupo de Dinâmica Orbital e Planetologia, CEP 12516-410, Guaratinguetá, SP, Brazil
[8] Université Côte d'Azur, Observatoire de la Côte d'Azur, CNRS, Laboratoire Lagrange, Bd de l'Observatoire, CS 34229, 06304 Nice Cedex 4, France
[9] Departamento de Astronomía, Universidad de Chile, Camino del Observatorio 1515, Las Condes, Santiago, Chile
[10] Instituto de Astrofísica de Andalucía, IAA-CSIC, Glorieta de la Astronomía s/n, 18008 Granada, Spain
[11] Universidade Federal do Rio de Janeiro - Observatório do Valongo, Ladeira Pedro Antônio 43, CEP 20.080-090 Rio de Janeiro - RJ, Brazil
[12] International Occultation Timing Association / European Section, Am Brombeerhag 13, D-30459 Hannover, Germany
[13] Internationale Amateursternwarte e.V. (IAS), Mittelstrasse 6, D-15749 Mittenwalde, Germany
[14] Institute for Astronomy, University of Edinburgh, Royal Observatory, Edinburgh EH9 3HJ, UK
[15] Florida Space Institute, University of Central Florida, 12354 Research Parkway, Partnership 1, Orlando, FL, USA
[16] BRAMON—Brazilian Meteor Observation Network, Nhandeara, Brazil.
[17] Grupo de Matemática Aplicada e Processamento de Sinais, State University of Mato Grosso do Sul - UEMS, Cassilândia, CEP 79540-000, MS, Brazil
[18] IATE-OAC, Universidad Nacional de Córdoba-CONICET, Laprida 854, X5000 BGR, Córdoba, Argentina
[19] Department of Physics, Chemistry and Material Science, University of Namibia, Private Bag 13301, Windhoek, Namibia
[20] Centre for Space Research, North-West University, Potchefstroom 2520, South Africa
[21] Association T60, Observatoire Midi-Pyrénées, 14 avenue Edouard Belin, 31400 Toulouse, France
[22] Southwest Research Institute, 1050 Walnut Street, Suite 300, Boulder, CO 80302, USA
[23] Dogsheaven Observatory, SMPW Q25 CJ1 LT10B Brasilia, Brazil
[24] Association of Argentine Observatories of Minor Bodies (AOACM))
[25] Centro de Astronomía (CITEVA), Universidad de Antofagasta, Av. Angamos 601, Antofagasta, Chile
[26] Ciel & Espace, Paris, France
[27] University of St Andrews, Centre for Exoplanet Science, SUPA School of Physics & Astronomy, North Haugh, St Andrews, KY16 9SS, United Kingdom
[28] Universidade Estadual de Ponta Grossa (UEPG), Ponta Grossa, Brazil
[29] Summit Kinetics Inc, United States
[30] Panamanian Observatory in San Pedro de Atacama - OPSPA
[31] Department of Physics, Southern University of Science and Technology, Shenzhen 518055, China
[32] Centro Brasileiro de Pesquisas Físicas, Rua Dr Xavier Sigaud 150, Rio de Janeiro 22290-180, Brazil
[33] Trans-Tasman Occultation Alliance (TTOA), Wellington PO Box 3181, New Zealand
[34] Association Réunionnaise pour l'Etude du Ciel Austral - ARECA, Sainte-Marie, La Réunion, France

[35] Institute of Astronomy, Faculty of Physics, Astronomy and Informatics, Nicolaus Copernicus University, Grudziadzka 5, 87-100, Torun, Poland

[36] Department of Astronomy and Space Science, Chungnam National University, 34134, Daejeon, Republic of Korea

[37] Observatório SONEAR, Brazil

[38] STAR Institute, Université de Liège, Allée du 6 août, 19C, 4000 Liège, Belgium

[39] Centre for ExoLife Sciences (CELS), Niels Bohr Institute, Øster Voldgade 5, 1350 Copenhagen, Denmark

[40] Astronomical Association of Queensland, 5 Curtis Street, Pimpama QLD 4209, Australia

[41] Department of Physics and Astronomy, University of North Carolina, Chapel Hill

[42] Central (Pulkovo) Observatory of the Russian Academy of Sciences, 196140, 65/1 Pulkovskoye Ave., Saint Petersburg, Russia

[43] Lowell Observatory, 1400 W Mars Hill Road, Flagstaff, AZ 86001, USA

[44] Massachusetts Institute of Technology, Department of Earth, Atmospheric and Planetary Sciences, 77 Massachusetts Avenue, Cambridge, MA 02139, USA)

[45] The Astronomical Research Institute, Ashmore, IL

[46] International Occultation Timing Association (IOTA), PO Box 7152, WA, 98042, USA

[47] NASA Johnson Space Center Astronomical Society, Houston, TX, USA

[48] Universidade Estadual do Oeste do Paraná (Unioeste), Avenida Tarquínio Joslin dos Santos 1300, Foz do Iguaçu, PR, 85870-650, Brazil

[49] Polo Astronômico Casimiro Montenegro Filho/FPTI-BR, Avenida Tancredo Neves 6731, Foz do Iguaçu, PR, 85867-900, Brazil

[50] San Pedro de Atacama Celestial Explorations - SPACE, Chile

[51] Comisión Nacional de Investigación y Desarrollo Aeroespacial del Perú - CONIDA, Luis Felipe Villarán 1069, San Isidro, Lima, Perú.

[52] Observatorio Astronómico de Moquegua, CP Cambrune, Carumas, Moquegua, Perú

[53] Physics and Astronomy Department, Appalachian State University, Boone, NC 28608, USA

[54] Astrocan Clube de Astronomia Nhandeara

[55] Centre for mathematical Plasma Astrophysics, Department of Mathematics, KU Leuven, Celestijnenlaan 200B, B-3001 Leuven, Belgium

[56] Centre for Electronic Imaging, Department of Physical Sciences, The Open University, Milton Keynes, MK7 6AA, UK

[57] Association Des Étoiles pour Tous, 19 Rue Saint Laurent, Maisoncelles, F-77320 Saint Martin du Boschet, France

[58] Observatorio Astronómico Córdoba UNC, Laprida 854, Córdoba, Argentina.

[59] (AGORA observatoire des Makes, AGORA, 18 Rue Georges Bizet, Observatoire des Makes, 97421 La Rivière, France

[60] Institute of Astrophysics, Pontificia Universidad Catolica de Chile, Av. Vicuña Mackenna 4860, Santiago, Chile

[61] Millennium Institute of Astrophysics, Chile

[62] Centre of Astro-Engineering, Pontificia Universidad Catolica de Chile, Av. Vicuña Mackenna 4860, Santiago, Chile.

[63] Department of Electrical Engineering, Pontificia Universidad Catolica de Chile, Av. Vicuña Mackenna 4860, Santiago, Chile

Appendix A: Observational circumstances

Table A.1 summarise the observational circumstances of each station for the eight stellar occultations presented here (name of station, coordinates, observers, telescope aperture, detector, band, exposure and cycle times, and the light curve Root Mean Square (RMS) noise. The status of each observation is mentioned (positive or negative detection of the main body, resolved, unresolved or no detection of the rings). Weather overcast and instrumental issues are also indicated.

Appendix B: Occultation maps

Figures B.1, B.2, B.3, B.4, B.5, B.6, B.7 and B.8 contain the occultation maps for the eight unpublished stellar occultations between 2017 and 2020. The maps were organised in inverse chronological order. The blue dots stand for the stations with a positive detection over the main body, the green dots are the ones with positive detections only for the rings, the yellow dots were stations with data that was unfit to detect the rings and negatives for the main body, and the red dots were stations without data covering the occultation instants (weather overcast or instrumental issues). The black dots stand for the centre of Chariklo every minute, and the big black dot represents the closest approach time. The solid black line stands for the path of Chariklo's shadow and the dashed line for the ring's shadow.

Appendix C: Occultation times and fitted parameters

Table C.1 lists the fitted times (immersion and emersion), duration of the event (Δt), apparent opacity (p', in sky plane) and minimum χ^2 per degree of freedom (χ^2_{pdf}) obtained for all the positive detections. The events are presented in reversed chronological order, and the detections are listed from northernmost to southernmost stations. The type of detection is mentioned: MB for Chariklo's main body, C1R and C2R for ring detections, for each we usually have a 1st and a 2nd (immersion and emersion) detections.

Table C.2 presents the rings parameters projected into the ring plane for each detection: the radial distance (r) to the ring centre (assumed to be circular), the radial width (W_r), normal opacity (p_N) and equivalent width (E_p). The number of datapoints within each detection (#) is also given, as well as the SNR of the observed stellar drops, i.e. the ratio of the stellar drop (one minus the bottom flux of the event, ϕ_0) and the RMS noise of the light curve.

Appendix D: Chariklo's updated positions

Stellar occultations provide precise astrometric position of the occulting body relative to the occulted star. If a new and more accurate position of the star is available, we can update the objects position (Rommel et al. 2020). Table 5 provides the solutions derived from seven stellar occultations observed between 2017 and 2020, using the Gaia Early Data Release 3 (GEDR3). Here, we also update results obtained from 12 occultations between 2013 and 2016 (Braga-Ribas et al. 2014; Bérard et al. 2017), using again the GEDR3.

Desmars et al. (2017) updated the positions obtained from pre-2017 events using the GDR2 catalogue. Let us consider Chariklo's previous position (α_c, δ_c), the GDR2 star position

($\alpha_{GDR2}, \delta_{GDR2}$) and the GEDR3 ($\alpha_{GEDR3}, \delta_{GEDR3}$), both at epoch. The updated Chariklo position (α'_c, δ'_c) is, then, obtained from

$$\alpha'_c = \alpha_c + \alpha_{GEDR3} - \alpha_{GDR2} \tag{D.1}$$
$$\delta'_c = \delta_c + \delta_{GEDR3} - \delta_{GDR2} \tag{D.2}$$

The updated Chariklo positions between 2013 and 2017 are given in Table D.1.

Appendix E: The case of the 2019-09-04 event in Hawaii

On 2019-09-04, Chariklo's system occulted a mag G 13.586 star as seen from Hawaii. A run was triggered to observe the event from the 8.1-m Gemini North telescope in Mauna Kea. Unfortunately, the weather only allowed the observations to start a few minutes after the occultation as can be seen in Figure E.1.

A simultaneous observation was set up at Mauna Loa, using a 0.36-m portable telescope. Due to a technical failure, the images were not recorded, but were being displayed on screen. The observers could use a smartphone to film the notebook screen, with the GPS time inserted in each frame, see Figure E.2.

As the smartphone video recording started after the occultation by the main body, only a transit of C1R in front of the star was eventually recorded. This atypical data-set was analysed using the aperture photometry package of `PyMovie` (Anderson 2019), resulting in the light curve shown in Figure E.3. As we could not retrieve the exact mid-time for each frame, we determined the immersion time using the time stamped in the images right before and after the star disappearance. We then consider that the mean time between the images with and without the star provides the immersion time, with an uncertainty of half the time between these two frames. The same protocol was followed to determine the emersion time.

The mid-time of the C1R occultation is then evaluated at UTC 08:02:38.993±0.017 s. The NIMA v.18 Chariklo's ephemeris having an uncertainty of 20 km for this event, this mid-time corresponds to a (f, g) position in the sky plane of (250.945 ± 20.0, −36.121 ± 20.0) km. The radial width of CR1 in the ring plane is then 6.77 ± 0.53 km, with normal opacity of 0.370 ± 0.094. These results are consistent with the obtained parameters from other occultations. If more observations of this event were to be obtained by other teams, the data presented here could be used to better constrain the geometry of this occultation.

Appendix F: Light curves

This section provides the plots of the normalised light curves vs. UTC analysed in this work. There are forty light curves obtained during the seven occultations observed between 2017 and 2020 (excluding the 2019-09-04 event). The events are listed in inverse chronological order, and the light curves are plotted from the northernmost to the southernmost stations. The date, event and observer are indicated in the title and label of each figure. The upper panel contains the complete normalised light curve (black dots) and the fitted model (red line). The bottom panels contain zoom-in views of a few seconds each centred on the detections of C1R and the immersions and emersions behind the main body, when detected.

Table A.1. Observational stations, technical details and circumstance.

Site Status Main Body Status Ring	Longitude Latitude Altitude	Observers	Telescope aperture Detector Filter	Exposure Time Cycle (s)	Light curve RMS (flux)
2020-06-19 – Australia					
Glenlee Positive Detection Unresolved Detection	150° 30' 01.6" E 23° 16' 10.1" S 50 m	S. Kerr	30 cm Watec 910BD Clear	0.640 0.640	0.138
2019-09-04 – Hawaii					
Gemini North – Mauna Kea Instrumental Issue	155° 28' 08.0" W 19° 49' 25.0" N 4184 m	F. Braga-Ribas	810 cm Andor/IXon-EM Blue-g / Red-i	0.040 0.040	0.019
Mauna Loa Instrumental Issue Resolved Detection[a]	155° 34' 34.9" W 19° 32' 10.6" N 3395 m	P. Maley C. Erickson	36 cm Watec 910HX Clear	0.017 0.017	0.127
2019-08-08 – La Réunion / Namibia					
Ste. Marie / La Réunion Positive Detection No Detection[b]	55° 34' 00.2" E 20° 53' 48.5" S 50 m	B. Mondon	28 cm QHY174M Clear	0.500 0.500	0.269
Ste. Marie / La Réunion Positive Detection No Detection	55° 31' 08.6" E 20° 54' 38.9" S 85 m	G. Hesler	40 cm QHY174M Clear	0.500 0.500	0.405
Maido / La Réunion Positive Detection No Detection	55° 23' 14.5" E 21° 04' 15.5" S 2195 m	T. Payet	30 cm ASI178MM Clear	0.500 0.500	0.286
Les Makes / La Réunion Positive Detection No Detection	55° 24' 36.3" E 21° 11' 56.1" S 990 m	P. Thierry	60 cm ASI178MM Clear	0.531 0.531	0.263
Langevin / La Réunion Positive Detection No Detection	55° 38' 47.7" E 21° 23' 12.0" S 20 m	F. Colas	28 cm ASI178MM Clear	0.333 0.333	0.290
Vastrap Guestfarm / Namibia Instrumental Issue	27° 44' 05.2" E 18° 25' 49.5" S 1090 m	M. Kretlow	40 cm Merlin/Raptor Clear	— —	—
2019-08-02 – Australia					
Yass Positive Detection No Detection	148° 58' 35.1" E 34° 51' 50.9" S 536 m	W. Hanna	51 cm QHY174GPS Clear	3.000 3.001	0.207
Murrumbateman Positive Detection No Detection	148° 59' 54.8" E 34° 57' 31.5" S 594 m	D. Herald	40 cm Watec 910BD Clear	1.280 1.280	0.204
Flynn No Detection No Detection	149° 02' 57.5" E 35° 11' 55.3" S 657 m	J. Newman	40 cm Watec 910BD Clear	1.280 1.280	0.532
2017-08-24 – Brazil					
OPD – Brazópolis Positive Detection Unresolved Detection	45° 34' 57.5" W 22° 32' 07.8" S 1864 m	J. I. B. Camargo F. Quispe-Huaynasi	160 cm Andor/IXon-EM Clear	0.500 0.513	0.063

[a] Due to instrumental issue the original data-set was lost, however a video recorded by the observer's smartphone was used to derive the immersion and emersion times of the second detection of the ring.

[b] No detection means that the data-set's features do not allowed the detection of Chariklo's rings.

Table A.1. [Cont.] Observational stations, technical details and circumstance.

Site	Longitude	Observers	Telescope aperture	Exposure Time	Light curve RMS
Status Main Body	Latitude		Detector	Cycle	(flux)
Status Ring	Altitude		Filter	(s)	

2017-07-23 – South America

Site	Longitude	Observers	Telescope aperture	Exposure Time	Light curve RMS
San Pedro de Atacama / Chile	68° 10' 44.0" W	N. Morales	41 cm	2.000	0.058
Negative Detection	22° 57' 14.0" S		SBIG STL11K3	4.370	
No Detection	2397 m		Clear		
San Pedro de Atacama / Chile	68° 10' 48.0" W	J. Fabrega	40 cm	1.000	0.099
Negative Detection	22° 57' 09.0" S		FLI PL16803	2.700	
Unresolved Detection	2396 m		Clear		
San Pedro de Atacama / Chile	68° 10' 48.0" W	J. F. Soulier	40 cm	3.000	0.023
Negative Detection	22° 57' 09.0" S		QHY9 CCD	7.000	
No Detection	2396 m		Clear		
San Pedro de Atacama / Chile	68° 10' 48.0" W	A. Maury	50 cm	3.000	0.045
Negative Detection	22° 57' 09.0" S		FLI13803	5.650	
No Detection	2396 m		Clear		
Cerro Burek / Argentina	69° 18' 25.0" W	N. Morales	45 cm	2.000	0.066
Negative Detection	31° 47' 12.0" S		SBIG STL11000	4.250	
No Detection	2665 m		Clear		
Ckoirama / Chile	69° 55' 49.0" W	J. P. Colque	60 cm	1.000	0.188
Negative Detection	24° 05' 21.0" S		FLI PL16801	2.569	
No Detection	0964 m		Clear		
VLT – Cerro Paranal / Chile	70° 24' 16.5" W	B. Sicardy	820 cm	0.100	0.027
Negative Detection	24° 37' 39.3" S		HAWK-I	0.100	
Resolved Detection	2635 m		K$_s$-band		
SSO^c – Cerro Paranal / Chile	70° 24' 16.5" W	E. Jehin	100 cm	1.200 / 1.200	0.020 / 0.013
Negative Detection	24° 37' 39.3" S		Andor/IKONL	2.000 / 2.040	
Unresolved Detection	2635 m		g' / I + z		
Tolar Grande / Argentina	67° 23' 43.6" W	M. Kretlow	41 cm	0.130	0.092
Negative Detection	24° 35' 23.5" S	R. A. Artola	Merlin/Raptor	0.130	
Resolved Detection	3524 m		Clear		
Cono de Arita / Argentina	67° 46' 00.2" W	M. D. Starck-Cuffini	25 cm	0.500	0.161
Positive Detection	25° 01' 59.8" S	M. V. Sieyra	ASI178MM	0.500	
No Detection	3532 m		Clear		
El Rodeo / Argentina	66° 08' 35.4" W	E. Meza	36 cm	0.150	0.358
Positive Detection	24° 52' 37.0" S	R. Melia	Merlin/Kite	0.170	
Unresolved Detection	3022 m		Clear		
Cachi Adentro / Argentina	66° 14' 16.7" W	E. M. Schneiter	36 cm	0.100	0.452
Positive Detection	25° 05' 33.9" S	C. Colazo	Merlin/Raptor	0.100	
No Detection	2684 m	M. Buie	Clear		
Augusto de Lima / Brazil	44° 04' 08.4" W	B. L. Giacchini	30 cm	1.000	0.174
Positive Detection	18° 01' 20.7" S	G. Benedetti-Rossi	Merlin/Raptor	1.000	
No Detection	0620 m		Clear		
El Salvador / Chile	69° 45' 03.8" W	J-L. Dauvergne	28 cm	0.050	0.318
Positive Detection	26° 18' 48.3" S		Merlin/Raptor	0.050	
Unresolved Detection	1607 m		Clear		
São José do Rio Preto / Brazil	49° 17' 52.2" W	R. Sfair	35 cm	1.000	0.213
Positive Detection	20° 42' 43.4" S	A. Amarante	Merlin/Raptor	1.000	
No Detection	0482 m	R. Poltronieri	Clear		
Inca de Oro / Chile	69° 54' 45.6" W	S. Bouley	25 cm	0.100	0.267
Positive Detection	26° 44' 45.3" S		Merlin/Raptor	0.100	
Unresolved Detection	1592 m		Clear		
Bilac / Brazil	50° 30' 20.9" W	L. S. Amaral	25 cm	6.000	0.150
Positive Detection	21° 23' 38.6" S		Canon T1i	11.000	
No Detection	0426 m		Clear		
Danish – La Silla / Chile	70° 44' 20.2" W	C. Snodgrass	154 cm	0.033 / 0.033	0.082 / 0.063
Negative Detection	29° 15' 21.3" S	T. C. Hinse	Lucky Imager	0.034 / 0.034	
Resolved Detection	2337 m	U. G. Jorgensen	Visual & Red^d		
		M. Dominik			
		J. Skottfelt			

^{c} The SSO observations were done at the telescopes Io and Europa.

^{d} The Danish dual experiment observed in the Visual (0.45-0.65 μm) and Red (0.7-1.0 μm) bands.

Table A.1. [Cont.] Observational stations, technical details and circumstance.

| Site Status Main Body Status Ring	Longitude Latitude Altitude	Observers	Telescope aperture Detector Filter	Exposure Time Cycle (s)	Light curve RMS (flux)
2017-07-23 – South America [Cont.]					
1m – La Silla / Chile Negative Detection Resolved Detection	70° 44' 20.2" W 29° 15' 21.3" S 2337 m	A. Zapata P. Torres	100 cm Merlin/Raptor Clear	0.100 0.100	0.074
TRAPPIST-South – La Silla / Chile Negative Detection Unresolved Detection	70° 44' 20.2" W 29° 15' 21.3" S 2337 m	E. Jehin	60 cm FLI PL3041-BB Clear	2.000 2.795	0.040
Foz do Iguaçu / Brazil Negative Detection No Detection	54° 35' 37.0" W 25° 26' 05.0" S 0184 m	D. I. Machado L. L. Trabuco	28 cm Merlin/Raptor Clear	4.000 4.000	0.038
OPD – Brazópolis / Brazil Negative Detection Resolved Detection	45° 34' 57.5" W 22° 32' 07.8" S 1864 m	F. Braga-Ribas F. L. Rommel	160 cm Andor/IXon-EM Clear	0.117 0.130	0.029
SARA – Cerro Tololo / Chile Negative Detection Resolved Detection	70° 48' 23.0" W 30° 10' 11.0" S 2207 m	R. Leiva S. Levine C. Zuluaga	60 cm FLI Clear	1.000 1.679	0.094
PROMPT^e – Cerro Tololo / Chile Negative Detection Resolved Detection	70° 48' 23.0" W 30° 10' 11.0" S 2207 m	J. Pollock V. Kouprianov D. Reichart T. Linder	40 cm AltaU-47 Clear	1.000 0.615	0.037
Oliveira / Brazil Weather Overcast	43° 59' 03.1" W 19° 52' 55.0" S 982 m	C. Jacques	45 cm ML FLI16803 Clear	— —	—
Guaratinguetá / Brazil Weather Overcast	45° 11' 25.0" W 22° 48' 34.0" S 0567 m	T. Santana T. Moura O. C. Winter T. Akemi	40 cm Merlin/Raptor Clear	— —	—
Brasília / Brazil Weather Overcast	47° 54' 39.9" W 15° 53' 29.9" S 1064 m	P. Cacella	50 cm ASI174MM Clear	— —	—
Ponta Grossa / Brazil Weather Overcast	50° 05' 56.6" W 25° 05' 22.5" S 910 m	C. L. Pereira M. Emilio	40 cm Merlin/Raptor Clear	— —	—
SOAR - Cerro Pachón / Chile Weather Overcast	70° 44' 21.1" W 30° 14' 16.9" S 2694 m	J. I. B. Camargo	410 cm Merlin/Raptor Clear	— —	—
2017-06-22 – Namibia					
Outeniqua Lodge Positive Detection Unresolved Detection	16° 49' 17.7" E 21° 17' 58.2" S 1416 m	F. Colas J. Desmars	25 cm Merlin/Raptor Clear	0.100 0.100	0.325
Onduruquea Guest Farm Positive Detection Resolved Detection	15° 59' 33.7" E 21° 36' 26.0" S 1220 m	M. Kretlow	50 cm Merlin/Raptor Clear	0.075 0.080	0.116
Windhoek Positive Detection Unresolved Detection	17° 06' 31.9" E 22° 41' 55.2" S 1902 m	M. Backes	35 cm Merlin/Raptor Clear	0.150 0.150	0.148
Windhoek Positive Detection Unresolved Detection	17° 06' 31.9" E 22° 41' 55.2" S 1902 m	E. Meza	40 cm ASI178MM Clear	0.200 0.203	0.151
Tivoli Lodge Positive Detection Unresolved Detection	18° 01' 01.2" E 23° 27' 40.2" S 1344 m	L. Maquet	40 cm Merlin/Raptor Clear	0.075 0.075	0.175
Hakos Negative Detection Resolved Detection	16° 21' 41.3" E 23° 14' 11.0" S 1843 m	W. Beisker	50 cm Merlin/Raptor Clear	0.050 0.050	0.122

The PROMPT observation were the combined data observed by P1, P3 and P5, allowing for a short cycle.

Table A.1. [Cont.] Observational stations, technical details and circumstance.

Site	Longitude	Observers	Telescope aperture	Exposure Time	Light curve RMS
Status Main Body	Latitude		Detector	Cycle	(flux)
Status Ring	Altitude		Filter	(s)	
2017-04-09 – Namibia					
Wabi Lodge	17° 32' 00.6" E	J. L. Dauvergne	30 cm	0.100	0.212
Positive Detection	20° 20' 38.9" S		Merlin/Raptor	0.100	
Resolved Detection	1382 m		Clear		
Weaver Rocks Lodge	16° 50' 29.9" E	M. Kretlow	50 cm	0.080	0.147
Positive Detection	20° 41' 56.3" S		Merlin/Raptor	0.080	
Resolved Detection	1647 m		Clear		
Hakos	16° 21' 42.0" E	K. L. Bath	50 cm	0.100	0.089
Negative Detection	23° 14' 10.0" S		Merlin/Raptor	0.100	
Resolved Detection^f	1881 m		Clear		

^{f} Only the second detection of the C1R was observed, due to the weather condition.
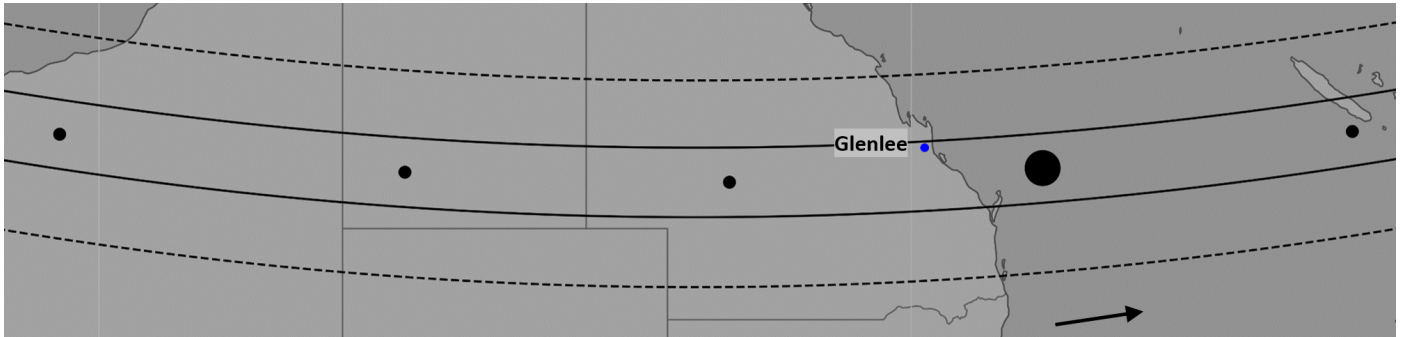
Fig. B.1. Occultation map for the 2020-06-19 event.
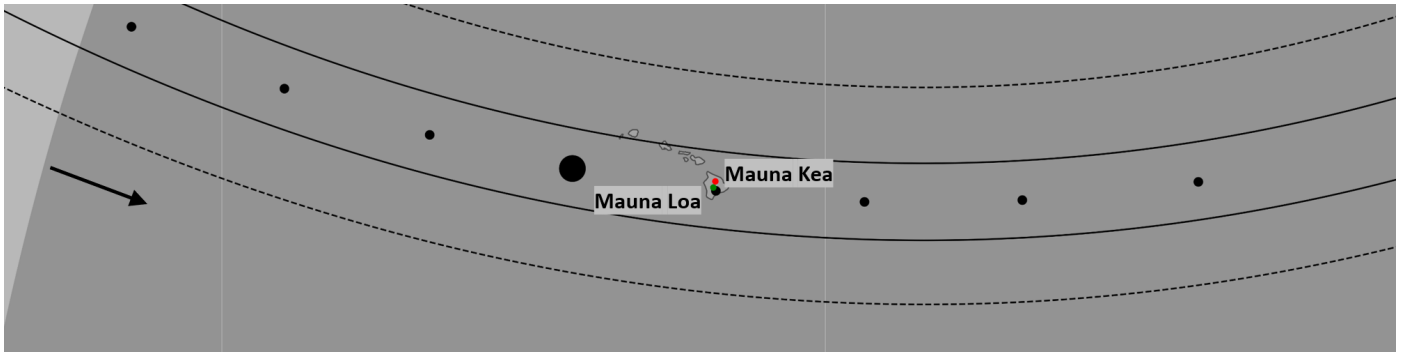
Fig. B.2. Occultation map for the 2019-09-04 event.
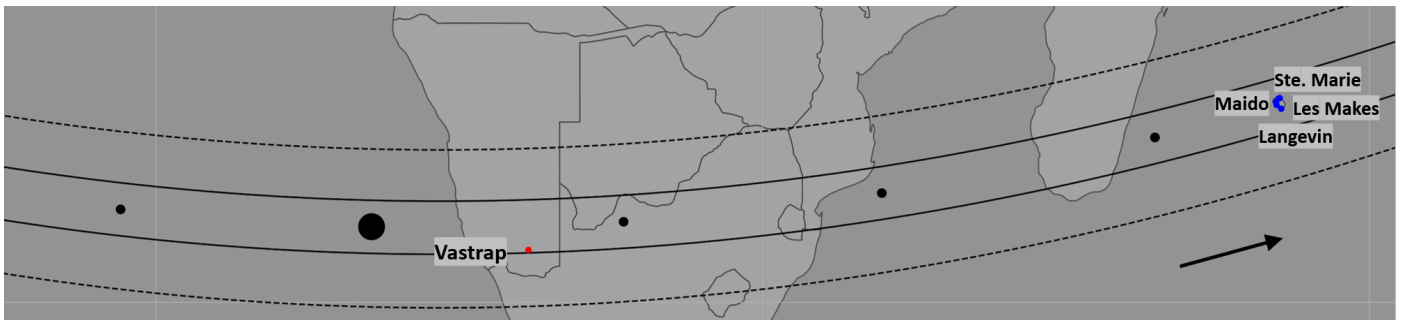
Fig. B.3. Occultation map for the 2019-08-08 event.
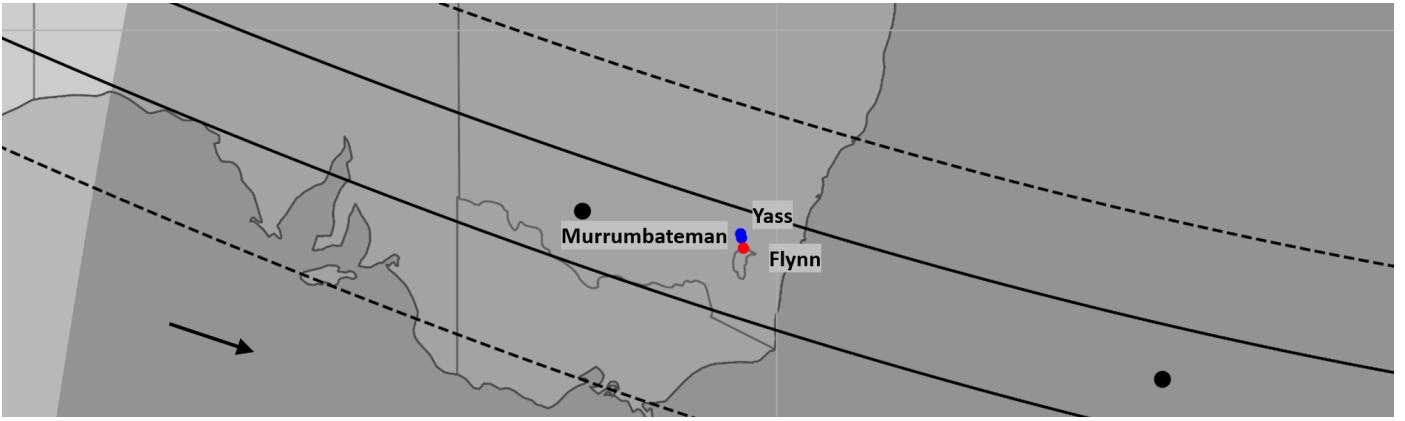
Fig. B.4. Occultation map for the 2019-08-02 event.
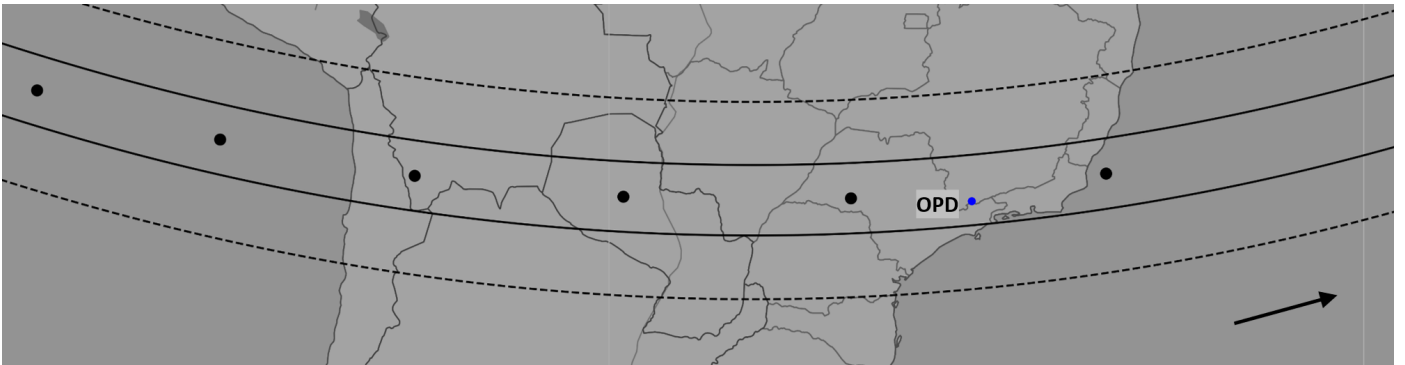
Fig. B.5. Occultation map for the 2017-08-24 event.
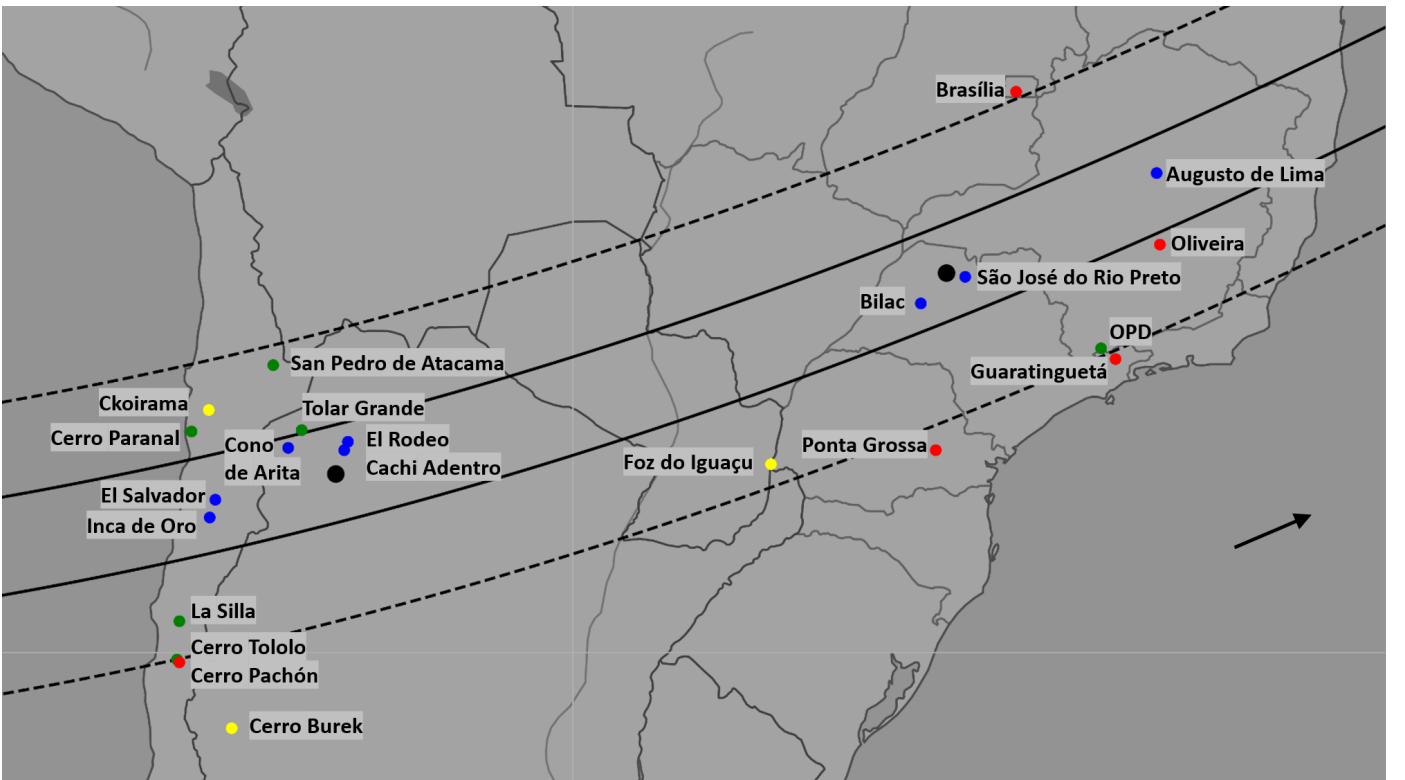
Fig. B.6. Occultation map for the 2017-07-23 event.
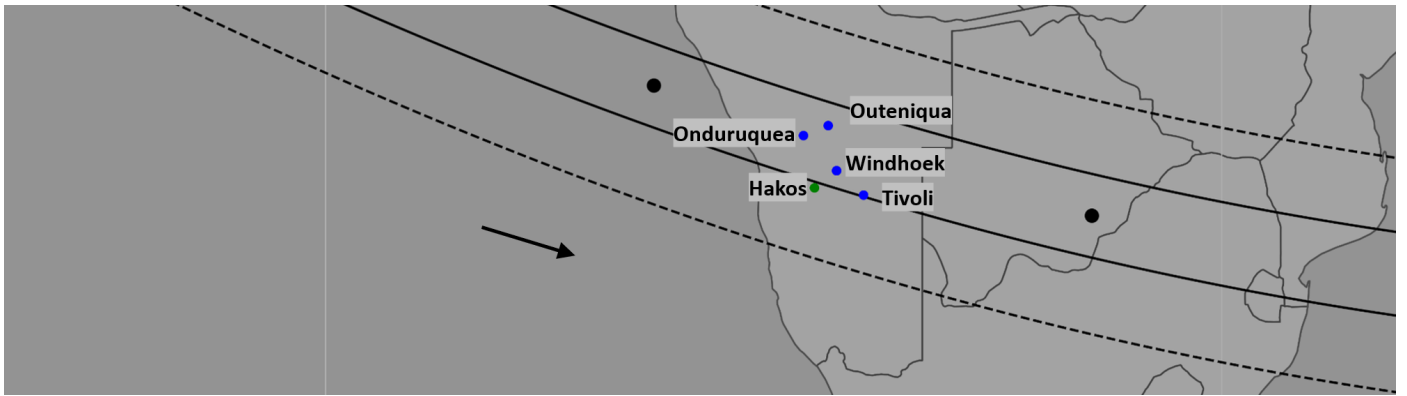
Fig. B.7. Occultation map for the 2017-06-22 event.
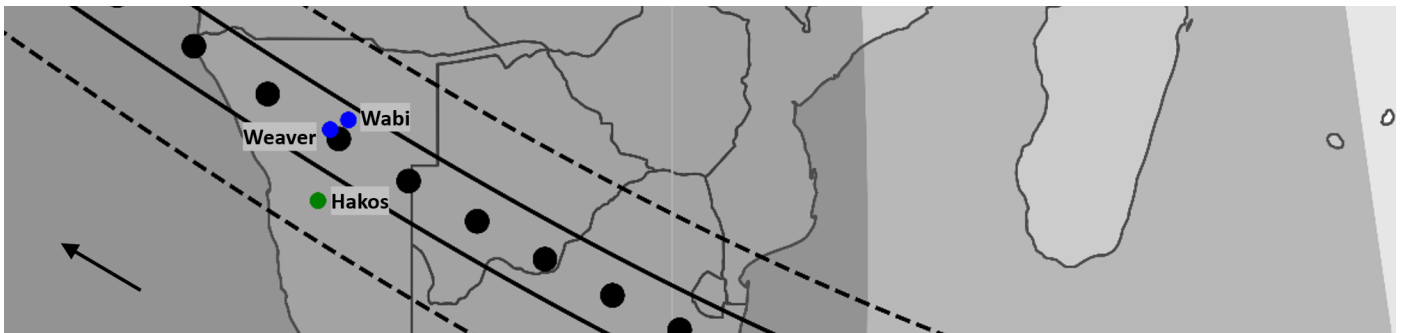
Fig. B.8. Occultation map for the 2019-09-04 event.

Table C.1. Fitted parameters obtained for each light curve with a positive detection.

Site	Detection	Immersion time (hh:mm:ss.sss)	Emersion time (hh:mm:ss.sss)	Duration (s)	Apparent opacity	χ^2_{pdf} (imm / eme)
2020-06-19 – Australia						
Glenlee	MB	15:51:51.770 (0.089)	15:51:59.334 (0.108)	07.564 (0.197)	1.000	0.978
	C1R 1st	15:51:37.601 (0.212)	15:51:39.584 (0.295)	01.983 (0.507)	0.225 (0.073)	0.920
	C1R 2nd	15:52:13.703 (0.337)	15:52:14.004 (0.296)	00.301 $\left(^{+0.633}_{-0.301}\right)$	0.696 $\left(^{+0.301}_{-0.543}\right)$	1.072
2019-08-08 – La Réunion / Namibia						
Ste. Marie - Mondon	MB	21:38:15.627 (0.223)	21:38:28.460 (0.140)	12.833 (0.363)	1.000	0.787 / 0.590
Ste. Marie - Hesler	MB	21:38:15.871 (0.244)	21:38:28.447 (0.320)	12.576 (0.564)	1.000	1.250 / 0.847
Maido	MB	21:38:16.659 (0.266)	21:38:29.231 (0.109)	12.572 (0.375)	1.000	1.349 / 1.427
Les Makes	MB	21:38:16.415 (0.144)	21:38:29.092 (0.146)	12.667 (0.290)	1.000	0.998 / 0.821
Langevin	MB	21:38:15.788 (0.094)	21:38:28.339 (0.102)	12.551 (0.196)	1.000	0.750 / 0.816
2019-08-02 – Australia						
Yass	MB	10:05:26.647 (0.371)	10:05:35.976 (0.885)	09.302 (1.256)	1.000	0.681 /1.170
Murrumbateman	MB	10:05:26.657 (0.421)	10:05:36.885 (0.405)	10.229 (0.826)	1.000	0.288 / 0.273
2017-08-24 – Brazil						
OPD	MB	02:54:17.122 (0.029)	02:54:35.957 (0.039)	18.834 (0.068)	1.000	0.795
	C1R 1st	02:54:03.343 (0.182)	02:54:04.058 (0.175)	00.715 (0.357)	0.782 $\left(^{+0.217}_{-0.548}\right)$	0.910
	C1R 2nd	02:54:48.556 (0.153)	02:54:49.019 (0.071)	00.462 (0.224)	0.286 $\left(^{+0.400}_{-0.056}\right)$	1.141
2017-07-23 – South America						
S. P. A. - Fabrega	C1R 2nd	05:55:59.034 (1.290)	05:56:01.222 (1.372)	02.188 $\left(^{+2.662}_{-2.188}\right)$	0.307 $\left(^{+0.693}_{-0.166}\right)$	1.385
VLT	C1R 1st	05:55:51.104 (0.004)	05:55:51.406 (0.008)	00.302 (0.012)	0.390 (0.014)	1.403
	C1R 2nd	05:56:14.242 (0.011)	05:56:14.532 (0.006)	00.290 (0.016)	0.429 (0.026)	1.074
	C2R 1st	05:55:50.568 (0.016)	05:55:50.740 (0.012)	00.172 (0.028)	0.057 (0.007)	1.873
	C2R 2nd	05:56:14.956 (0.055)	05:56:15.011 (0.055)	00.055 $\left(^{+0.110}_{-0.055}\right)$	0.803 $\left(^{+0.196}_{-0.760}\right)$	0.968
SSO	C1R 1st	05:55:50.836 (0.263)	05:55:51.474 (0.243)	00.637 (0.506)	0.949 $\left(^{+0.048}_{-0.847}\right)$	1.761
	C1R 2nd	05:56:14.242 (0.215)	05:56:14.731 (0.068)	00.288 (0.022)	0.755 $\left(^{+0.187}_{-0.597}\right)$	1.197
Tolar Grande	C1R 1st	05:55:37.371 (0.026)	05:55:37.721 (0.040)	00.350 (0.066)	0.271 (0.057)	1.009
	C1R 2nd	05:56:03.775 (0.022)	05:56:04.017 (0.026)	00.242 (0.049)	0.444 (0.090)	1.132
Cono de Arita	MB	05:55:48.909 (0.070)	05:55:56.175 (0.074)	06.955 (0.160)	1.000	0.826
El Rodeo	MB	05:55:41.690 (0.076)	05:55:50.631 (0.091)	08.941 (0.167)	1.000	0.911
	C1R 1st	05:55:31.878 (0.288)	05:55:32.374 (0.069)	00.496 (0.357)	0.442 $\left(^{+0.533}_{-0.236}\right)$	0.955
	C1R 2nd	05:55:59.265 (0.107)	05:55:59.819 (0.107)	00.554 (0.214)	0.228 $\left(^{+0.178}_{-0.096}\right)$	0.888
Cachi Adentro	MB	05:55:41.300 (0.062)	05:55:51.360 (0.052)	10.060 (0.114)	1.000	0.882
Augusto de Lima	MB	05:54:24.294 (0.270)	05:54:35.248 (0.215)	10.955 (0.485)	1.000	0.912
El Salvador	MB	05:55:54.242 (0.027)	05:56:06.002 (0.021)	11.760 (0.049)	1.000	0.826
	C1R 1st	05:55:45.710 (0.033)	05:55:46.009 (0.017)	00.299 (0.049)	0.590 (0.185)	0.954
	C1R 2nd	05:56:14.349 (0.056)	05:56:14.660 (0.140)	00.311 (0.196)	0.324 (0.182)	0.944
São J. Rio Preto	MB	05:54:39.593 (0.202)	05:54:51.875 (0.201)	12.282 (0.403)	1.000	1.123
Inca de Oro	MB	05:55:54.765 (0.026)	05:56:06.951 (0.026)	12.186 (0.052)	1.000	0.838
	C1R 1st	05:55:46.430 (0.043)	05:55:46.651 (0.121)	00.220 (0.163)	0.396 $\left(^{+0.437}_{-0.242}\right)$	1.296
	C1R 2nd	05:56:15.079 (0.027)	05:56:15.210 (0.025)	00.131 (0.053)	0.559 $\left(^{+0.346}_{-0.192}\right)$	0.903
Bilac	MB	05:54:46.233 (3.876)	05:54:56.465 (2.694)	10.232 (6.569)	1.000	0.552
Danish Visual	C1R 1st	05:55:54.536 (0.004)	05:55:54.874 (0.006)	00.338 (0.010)	0.423 (0.025)	1.123
	C1R 2nd	05:56:13.750 (0.011)	05:56:14.183 (0.008)	00.433 (0.020)	0.458 (0.029)	1.433
	C2R 1st	05:55:53.887 (0.010)	05:55:53.914 (0.012)	00.027 (0.022)	0.588 (0.362)	0.994
	C2R 2nd	05:56:14.868 (0.005)	05:56:14.883 (0.006)	00.015 (0.011)	0.723 (0.266)	1.101

Table C.1. [Cont.] Fitted parameters obtained for each light curve with a positive detection.

Site	Detection	Immersion time (hh:mm:ss.sss)	Emersion time (hh:mm:ss.sss)	Duration (s)	Apparent opacity	χ^2_{pdf} (imm / eme)
2017-07-23 – South America [Cont.]						
Danish Red	C1R 1st	05:55:54.539 (0.004)	05:55:54.861 (0.005)	00.322 (0.009)	0.377 (0.018)	1.077
	C1R 2nd	05:56:13.752 (0.008)	05:56:14.193 (0.005)	00.440 (0.013)	0.365 (0.018)	1.436
	C2R 1st	05:55:53.838 (0.013)	05:55:53.924 (0.015)	00.086 (0.028)	0.115 (0.039)	0.957
	C2R 2nd	05:56:14.822 (0.006)	05:56:14.862 (0.008)	00.040 (0.014)	0.213 (0.036)	0.904
1m – La Silla	C1R 1st	05:55:54.519 (0.013)	05:55:54.855 (0.018)	00.336 (0.031)	0.394 (0.037)	1.096
	C1R 2nd	05:56:13.745 (0.010)	05:56:14.226 (0.011)	00.481 (0.021)	0.386 (0.028)	1.398
TRAPPIST-South	C1R 1st	05:55:54.498 (1.366)	05:55:55.994 (1.743)	01.495 $(^{+3.110}_{-1.495})$	0.067 $(^{+0.890}_{-0.018})$	1.131
	C1R 2nd	05:56:12.782 (1.403)	05:56:14.072 (1.498)	01.291 $(^{+2.902}_{-1.291})$	0.506 $(^{+0.471}_{-0.448})$	1.103
OPD	C1R 1st	05:54:29.963 (0.009)	05:54:30.731 (0.007)	00.769 (0.016)	0.381 (0.016)	2.155
	C1R 2nd	05:54:39.651 (0.006)	05:54:40.534 (0.008)	00.883 (0.014)	0.386 (0.012)	2.909
	C2R 1st	05:54:28.778 (0.019)	05:54:28.872 (0.027)	00.094 (0.045)	0.214 (0.104)	1.243
	C2R 2nd	05:54:41.699 (0.004)	05:54:41.710 (0.004)	00.011 (0.008)	0.978 $(^{+0.020}_{-0.115})$	2.588
SARA	C1R^c	05:56:02.499 (0.205)	05:56:06.988 (0.041)	04.488 (0.246)	0.379 (0.014)	1.113
PROMPT	C1R^c	05:56:02.260 (0.043)	05:56:07.228 (0.107)	04.968 (0.150)	0.373 (0.016)	2.205
2017-06-22 – Namibia						
Outeniqua Lodge	MB	21:21:20.179 (0.032)	21:21:30.193 (0.034)	10.013 (0.066)	1.000	0.897 / 0.905
	C1R 1st	21:21:11.469 (0.048)	21:21:11.768 (0.053)	00.299 (0.101)	0.527 $(^{+0.472}_{-0.170})$	0.781
	C1R 2nd	21:21:39.450 (0.044)	21:21:39.745 (0.037)	00.295 (0.081)	0.633 $(^{+0.367}_{-0.227})$	0.979
Onduruquea G. F.	MB	21:21:22.023 (0.010)	21:21:33.634 (0.011)	11.610 (0.021)	1.000	0.809 / 0.593
	C1R 1st	21:21:13.486 (0.012)	21:21:13.702 (0.015)	00.216 (0.027)	0.453 (0.063)	1.058
	C1R 2nd	21:21:42.047 (0.014)	21:21:42.251 (0.012)	00.204 (0.026)	0.403 (0.059)	0.946
Windhoek - Backes	MB	21:21:17.234 (0.024)	21:21:27.189 (0.026)	09.955 (0.050)	1.000	0.897 / 1.124
	C1R 1st	21:21:07.646 (0.067)	21:21:07.898 (0.069)	00.252 (0.136)	0.352 $(^{+0.647}_{-0.080})$	0.884
	C1R 2nd	21:21:35.709 (0.052)	21:21:36.082 (0.076)	00.376 (0.128)	0.225 $(^{+0.118}_{-0.067})$	1.552
Windhoek - Meza	MB	21:21:17.288 (0.028)	21:21:27.228 (0.034)	09.940 (0.062)	1.000	1.015 / 1.187
	C1R 1st	21:21:07.718 (0.076)	21:21:07.976 (0.122)	00.258 (0.198)	0.247 $(^{+0.752}_{-0.083})$	0.988
	C1R 2nd	21:21:35.825 (0.039)	21:21:35.968 (0.046)	00.143 (0.085)	0.970 $(^{+0.030}_{-0.528})$	1.430
Tivoli Lodge	MB	21:21:15.478 (0.011)	21:21:19.838 (0.038)	04.361 (0.049)	1.000	0.522 / 0.817
	C1R 1st	21:21:03.630 (0.031)	21:21:03.834 (0.038)	00.139 (0.069)	0.412 $(^{+0.581}_{-0.122})$	0.821
	C1R 2nd	21:21:30.580 (0.036)	21:21:30.724 (0.018)	00.144 (0.054)	0.517 $(^{+0.383}_{-0.140})$	0.920
Hakos	C1R 1st	21:21:10.218 (0.007)	21:21:10.426 (0.007)	00.208 (0.014)	0.433 (0.049)	1.136
	C1R 2nd	21:21:36.347 (0.011)	21:21:36.570 (0.007)	00.223 (0.018)	0.390 (0.042)	0.780
2017-04-09 – Namibia						
Wabi Lodge	MB	02:11:36.536 (0.023)	02:12:16.672 (0.021)	40.154 (0.044)	1.000	0.640 / 0.593
	C1R 1st	02:10:45.861 (0.045)	02:10:47.259 (0.087)	01.398 (0.132)	0.304 (0.044)	1.085
	C1R 2nd	02:13:00.816 (0.054)	02:13:01.868 (0.053)	01.052 (0.107)	0.410 (0.056)	0.975
Weaver R. L.	MB	02:11:20.357 (0.010)	02:12:15.199 (0.013)	54.850 (0.023)	1.000	1.002 / 0.968
	C1R 1st	02:10:38.477 (0.022)	02:10:39.737 (0.024)	01.260 (0.046)	0.361 (0.024)	1.078
	C1R 2nd	02:12:56.960 (0.023)	02:12:57.986 (0.007)	01.026 (0.030)	0.511 (0.029)	0.909
Hakos	C1R 2nd	02:13:09.054 (0.026)	02:13:10.345 (0.020)	01.291 (0.047)	0.518 (0.032)	1.246

^{c} The observations at Cerro Tololo (SARA and PROMPT) were grazing over C1R, meaning that only one detection were made.

Note: MB stands for the Main Body detections, C1R and C2R for the rings detections. As each transit of the ring in front of the star is considered as a detection, a given light curve may detect twice that ring (SNR allowing) during a given event. For the main body occultations the apparent opacity was not fitted and fixed as 1 (opaque body).

Table C.2. Fitted ring parameters in the ring plane obtained for each light curve.

Site	Detec.	r (km)	W_r (km)	p_N	E_p (km)	#	$\frac{(1-\phi_0)}{RMS}$
			C1R				
			2020-06-19 – Australia				
Glenlee	1st	392.402 (10.723)	40.396 (8.286)	0.177 $(^{+0.076}_{-0.048})$	7.192 $(^{+2.381}_{-1.602})$	03	02.83
	2nd	384.352 (11.825)	6.465 $(^{+10.634}_{-02.946})$	0.590 $(^{+0.255}_{-0.460})$	3.814 $(^{+1.956}_{-2.148})$	01	03.22
			2017-08-24 – Brazil				
OPD	1st	391.700 (6.109)	9.807 $(^{+1.724}_{-5.492})$	0.214 $(^{+0.534}_{-0.042})$	2.103 $(^{+1.769}_{-0.296})$	02	02.98
	2nd	384.245 (3.826)	6.465 $(^{+10.634}_{-2.946})$	0.590 $(^{+0.255}_{-0.460})$	3.814 $(^{+1.956}_{-2.148})$	01	02.88
			2017-07-23 – South America				
SPA - Fabrega	2nd	394.185 $(^{+36.059}_{-25.198})$	27.151 $(^{+33.033}_{-27.151})$	0.234 $(^{+0.529}_{-0.127})$	18.137 $(^{+2.611}_{-16.683})$	01	04.01
VLT	1st	386.211 (0.267)	6.596 (0.262)	0.297 (0.009)	1.959 (0.140)	04	23.52
	2nd	386.274 (0.355)	6.524 (0.360)	0.327 (0.020)	2.133 (0.255)	03	24.44
SSO	1st	388.432 (11.337)	7.920 $(^{+14.125}_{-3.701})$	0.394 $(^{+0.362}_{-0.267})$	3.118 $(^{+0.861}_{-1.287})$	02	07.65
	2nd	388.507 (0.491)	4.760 $(^{+12.671}_{-0.122})$	0.749 $(^{+0.012}_{-0.637})$	3.565 $(^{+0.090}_{-1.658})$	02	08.90
Tolar Grande	1st	391.109 (1.646)	8.670 (1.635)	0.207 (0.043)	1.795 (0.782)	03	04.74
	2nd	390.969 (1.222)	6.068 (1.229)	0.339 (0.069)	2.057 (0.920)	03	07.33
El Rodeo	1st	384.165 (9.431)	7.920 $(^{+14.125}_{-3.701})$	0.394 $(^{+0.362}_{-0.267})$	3.118 $(^{+0.861}_{-1.287})$	03	02.61
	2nd	384.024 (5.652)	15.103 $(^{+4.076}_{-3.993})$	0.199 $(^{+0.108}_{-0.100})$	3.004 $(^{+1.295}_{-1.346})$	04	01.75
El Salvador	1st	390.513 (1.331)	7.811 $(^{+1.367}_{-0.824})$	0.388 $(^{+0.187}_{-0.088})$	3.033 $(^{+1.428}_{-0.570})$	07	02.62
	2nd	390.095 (5.325)	5.390 $(^{+7.818}_{-1.695})$	0.243 $(^{+0.159}_{-0.137})$	1.307 $(^{+0.854}_{-0.530})$	06	01.72
Inca de Oro	1st	390.145 (4.428)	6.614 $(^{+2.553}_{-4.898})$	0.228 $(^{+0.512}_{-0.094})$	1.510 $(^{+0.621}_{-0.714})$	03	02.35
	2nd	389.436 (1.440)	3.915 $(^{+1.020}_{-1.561})$	0.394 $(^{+0.366}_{-0.126})$	1.542 $(^{+1.077}_{-0.423})$	03	03.29
Danish Visual	1st	386.747 (0.185)	6.064 (0.179)	0.323 (0.019)	1.959 (0.176)	11	08.22
	2nd	385.576 (0.369)	8.191 (0.378)	0.349 (0.022)	2.859 (0.320)	14	08.60
Danish Red	1st	386.840 (0.167)	5.779 (0.162)	0.288 (0.014)	1.664 (0.130)	12	09.75
	2nd	385.686 (0.240)	8.326 (0.246)	0.278 (0.014)	2.315 (0.188)	15	09.62
1m – La Silla	1st	387.081 (0.573)	6.035 (0.557)	0.300 (0.028)	1.811 (0.352)	03	08.59
	2nd	385.908 (0.388)	9.107 (0.398)	0.294 (0.021)	2.677 (0.317)	05	08.42
TRAPPIST-South	1st	376.900 $(^{+60.358}_{-49.445})$	25.448 $(^{+57.334}_{-22.207})$	0.475 $(^{+0.287}_{-0.440})$	12.099 $(^{+7.152}_{-10.784})$	01	02.95
	2nd	375.774 $(^{+55.900}_{-46.330})$	19.586 $(^{+57.596}_{-16.672})$	0.608 $(^{+0.154}_{-0.575})$	11.918 $(^{+5.874}_{-10.760})$	01	02.85
OPD	1st	385.321 (0.149)	6.456 (0.134)	0.291 (0.012)	1.879 (0.118)	07	21.10
	2nd	385.441 (0.131)	8.920 (0.141)	0.294 (0.009)	2.622 (0.123)	08	21.41
SARA	[a]	388.928 $(^{+0.931}_{-0.852})$	>4.443 (0.244)	0.289 (0.011)	>1.284 (0.122)	03	06.58
PROMPT	[a]	389.823 $(^{+0.682}_{-0.405})$	>4.819 (0.146)	0.284 (0.012)	>1.369 (0.101)	09	16.38
			2017-06-22 – Namibia				
Outeniqua	1st	388.073 (2.716)	8.266 $(^{+1.972}_{-2.750})$	0.410 $(^{+0.367}_{-0.132})$	3.391 $(^{+2.654}_{-1.081})$	04	02.45
	2nd	390.936 (2.179)	8.104 $(^{+1.706}_{-1.880})$	0.492 $(^{+0.285}_{-0.177})$	3.989 $(^{+2.919}_{-1.370})$	04	02.65
Onduruquea	1st	391.014 (0.739)	5.891 $(^{+0.441}_{-0.636})$	0.360 $(^{+0.042}_{-0.057})$	2.121 $(^{+0.179}_{-0.351})$	03	06.09
	2nd	390.503 (0.711)	5.550 $(^{+0.532}_{-0.486})$	0.314 $(^{+0.045}_{-0.047})$	1.744 $(^{+0.239}_{-0.260})$	03	05.28
Wdh - Backes	1st	393.714 (3.655)	7.459 $(^{+2.267}_{-3.973})$	0.274 $(^{+0.504}_{-0.062})$	2.045 $(^{+1.514}_{-0.381})$	02	05.51
	2nd	389.827 (3.439)	9.987 $(^{+2.967}_{-2.690})$	0.175 $(^{+0.092}_{-0.052})$	1.746 $(^{+0.560}_{-0.416})$	03	03.90
Wdh - Meza	1st	391.699 (5.323)	8.189 $(^{+3.029}_{-6.027})$	0.193 $(^{+0.585}_{-0.064})$	1.577 $(^{+1.340}_{-0.590})$	02	03.01
	2nd	389.881 (2.284)	3.731 $(^{+2.011}_{-0.731})$	0.755 $(^{+0.023}_{-0.411})$	2.816 $(^{+0.810}_{-1.172})$	01	04.82
Tivoli	1st	391.348 (1.781)	3.872 $(^{+1.269}_{-2.034})$	0.320 $(^{+0.452}_{-0.095})$	1.240 $(^{+0.388}_{-0.334})$	02	03.43
	2nd	390.145 (1.394)	3.909 $(^{+1.008}_{-1.561})$	0.402 $(^{+0.298}_{-0.109})$	1.571 $(^{+0.489}_{-0.382})$	03	04.04
Hakos	1st	387.490 (0.350)	5.095 $(^{+0.273}_{-0.197})$	0.342 $(^{+0.033}_{-0.043})$	1.740 $(^{+0.202}_{-0.176})$	04	05.57
	2nd	393.668 (0.452)	5.558 $(^{+0.365}_{-0.426})$	0.313 $(^{+0.031}_{-0.043})$	1.739 $(^{+0.125}_{-0.250})$	04	05.11

[a] As we have a grazing detection at SARA and PROMPT, we give a lower limit to the radial width.

Table C.2. [Cont.] Fitted ring parameters in the ring plane obtained for each light curve.

Site	Detec.	r (km)	W_r (km)	p_N	E_p (km)	#	$\frac{(1-\phi_0)}{RMS}$
C1R							
2017-04-09 – Namibia							
Wabi Lodge	1st	386.859 (0.635)	7.056 (0.258)	0.241 (0.035)	1.700 (0.318)	16	02.43
	2nd	389.603 (0.565)	5.725 (0.167)	0.326 (0.044)	1.866 (0.314)	12	03.07
Weaver R. L.	1st	388.185 (0.240)	7.591 (0.717)	0.287 (0.019)	2.179 (0.364)	18	04.02
	2nd	387.684 (0.218)	5.712 (0.581)	0.406 (0.023)	2.319 (0.381)	15	05.18
Hakos	2nd	388.314 (0.200)	5.642 (0.205)	0.411 (0.025)	2.319 (0.230)	16	08.63
C2R							
2017-07-23 – South America							
VLT	1st	401.125 (0.630)	3.716 $\left(^{+0.631}_{-0.527}\right)$	0.045 $\left(^{+0.005}_{-0.006}\right)$	0.168 $\left(^{+0.016}_{-0.020}\right)$	02	04.26
	2nd	400.790 (0.248)	0.159 $\left(^{+3.110}_{-0.097}\right)$	0.664 $\left(^{+0.099}_{-0.631}\right)$	0.105 $\left(^{+0.096}_{-0.061}\right)$	01	04.05
Danish Visual	1st	400.417 (0.425)	0.277 $\left(^{+0.640}_{-0.129}\right)$	0.445 $\left(^{+0.317}_{-0.294}\right)$	0.123 $\left(^{+0.036}_{-0.026}\right)$	04	02.65
	2nd	400.944 (0.213)	0.258 $\left(^{+0.161}_{-0.072}\right)$	0.598 $\left(^{+0.158}_{-0.264}\right)$	0.154 $\left(^{+0.039}_{-0.034}\right)$	04	04.08
Danish Red	1st	400.805 (0.543)	0.191 $\left(^{+1.233}_{-0.073}\right)$	0.500 $\left(^{+0.212}_{-0.420}\right)$	0.095 $\left(^{+0.021}_{-0.016}\right)$	04	02.96
	2nd	400.286 (0.504)	0.801 $\left(^{+0.440}_{-0.559}\right)$	0.158 $\left(^{+0.282}_{-0.056}\right)$	0.127 $\left(^{+0.029}_{-0.035}\right)$	04	02.70
OPD	1st	399.263 (0.530)	0.631 $\left(^{+0.545}_{-0.185}\right)$	0.152 $\left(^{+0.067}_{-0.073}\right)$	0.096 $\left(^{+0.015}_{-0.012}\right)$	01	05.75
	2nd	400.301 (0.095)	0.095 $\left(^{+0.015}_{-0.010}\right)$	0.759 $\left(^{+0.002}_{-0.091}\right)$	0.072 $\left(^{+0.010}_{-0.009}\right)$	02	03.78

Note: The radial distance (r) to the ring centre (assumed to be circular), the radial width (W_r), normal opacity (p_N) and equivalent width (E_p). There is also the number of data points within the detection. Lastly there is the ratio of bottom flux over the RMS of each light curve, that can be used to quantify the SNR of the detection.

Table D.1. Update of astrometrical Chariklo's positions for the events observed between 2013 and 2016.

Date and time UTC	Right Ascension	Declination
2013-06-03 06:25:30.000	$16^h\ 56^m\ 06^s.5117522$	-40° 31' 30".107042
2014-02-16 07:45:35.000	$17^h\ 35^m\ 55^s.2915296$	-38° 05' 17".300445
2014-03-16 20:31:45.000	$17^h\ 40^m\ 39^s.8348967$	-38° 25' 46".483279
2014-04-29 23:14:12.000	$17^h\ 39^m\ 02^s.1051292$	-38° 52' 48".749358
2014-06-28 22:24:35.000	$17^h\ 24^m\ 50^s.3869110$	-38° 41' 05".485778
2015-04-26 02:11:58.000	$18^h\ 10^m\ 46^s.1055222$	-36° 38' 56".597743
2015-05-12 17:55:40.000	$18^h\ 08^m\ 29^s.3099452$	-36° 44' 56".801226
2016-07-26 00:00:00.000	$18^h\ 20^m\ 35^s.3610788$	-34° 02' 29".041382
2016-08-10 14:23:00.000	$18^h\ 17^m\ 47^s.3503443$	-33° 51' 02".478041
2016-08-10 16:43:00.000	$18^h\ 17^m\ 46^s.4742139$	-33° 50' 57".707107
2016-08-15 11:38:00.000	$18^h\ 17^m\ 06^s.2478821$	-33° 46' 56".499075
2016-10-01 10:10:00.000	$18^h\ 16^m\ 20^s.0944710$	-33° 01' 10".842803
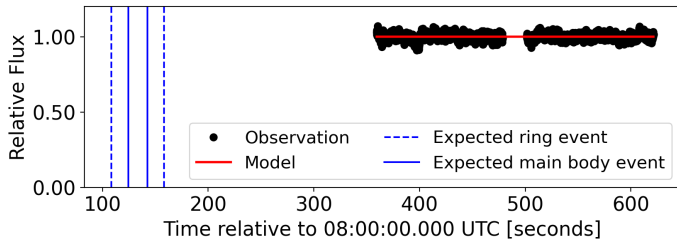
Fig. E.1. Light curve obtained at Gemini North on 2017-07-23. The solid blue vertical lines stands for the expected times for the main body occultation and the dashed lines for the expected times for the ring. The black points are the data points, which were taken in two blocks separated by a few seconds. See text for details.
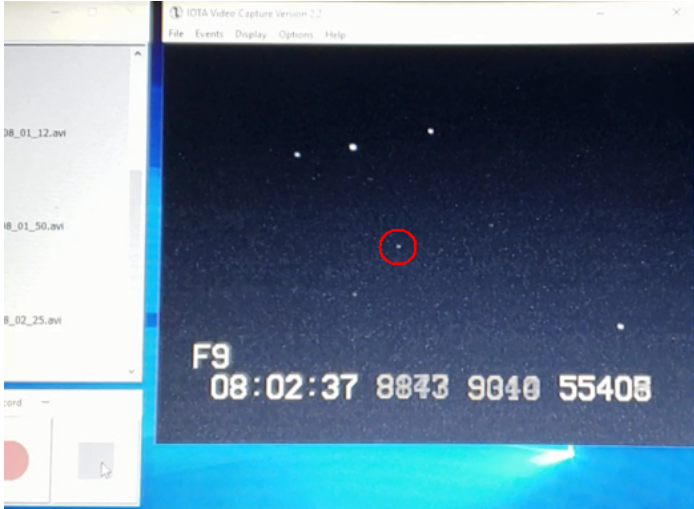
Fig. E.2. One frame from the smartphone video of the notebook screen, during the 2019-09-04 event. The occulted star is highlighted by the red circle.
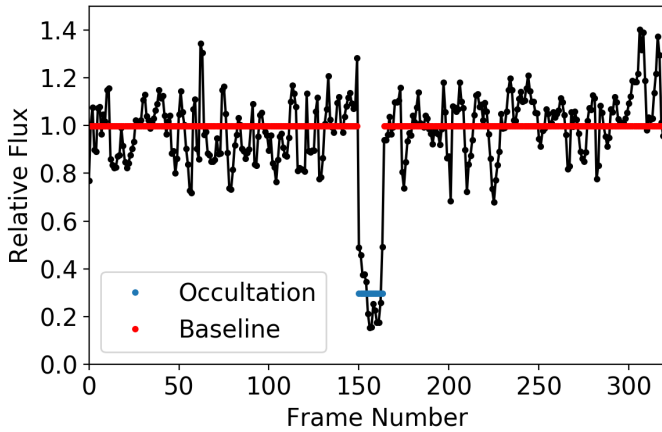
Fig. E.3. Normalised flux vs. frame number obtained at Mauna Loa during the 2019-09-04 event, showing the occultation by C1R. The red line stands for the baseline flux (1.0).
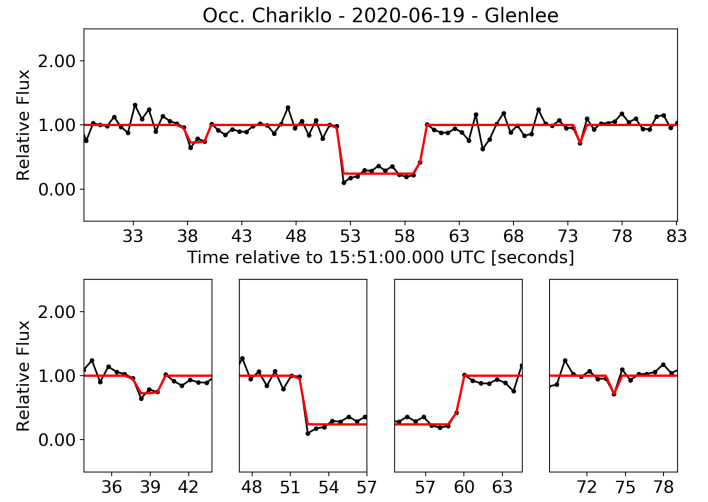
Fig. F.1. Light curve obtained in Glenlee on 2020-06-19. The event, date and observer are indicated in the title and label. The upper panel contains the complete normalised light curve (black dots) and the fitted model (red line). The bottom panels contain zoom-in views of a few seconds each centred on the detections of C1R and the immersions and emersions behind the main body.
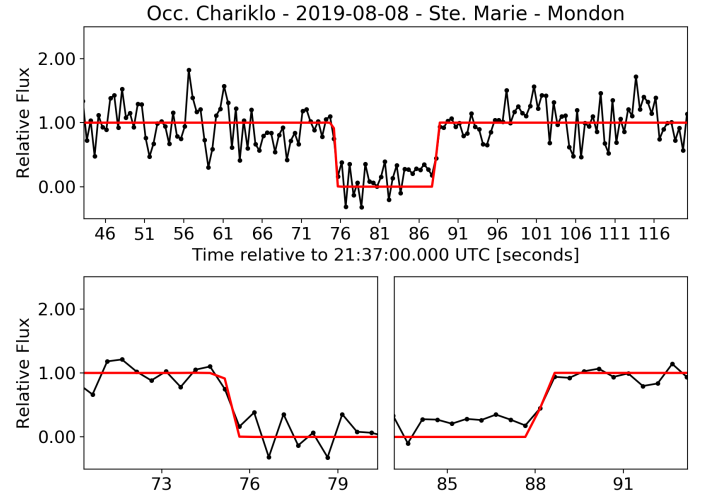
Fig. F.2. Light curve obtained at Ste. Marie by Mondon on 2019-08-08.
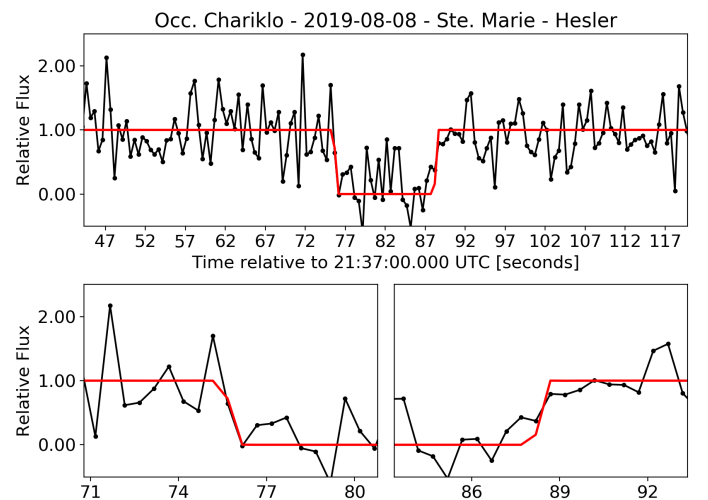
Fig. F.3. Light curve obtained at Ste. Marie by Hesler on 2019-08-08.
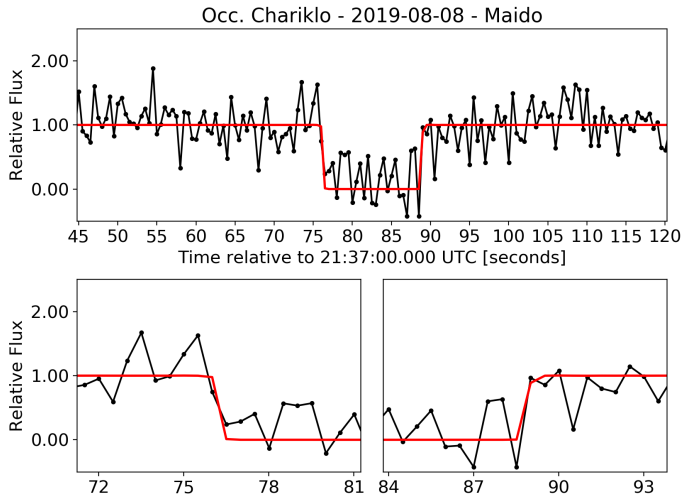
Fig. F.4. Light curve obtained at Maido on 2019-08-08.
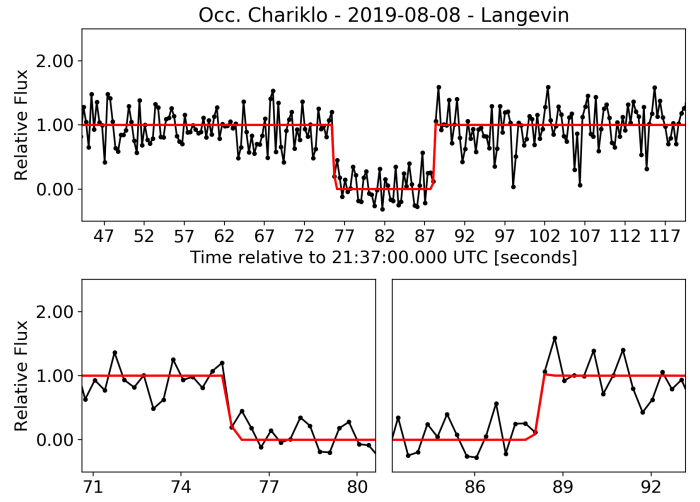
Fig. F.6. Light curve obtained at Langevin on 2019-08-08.
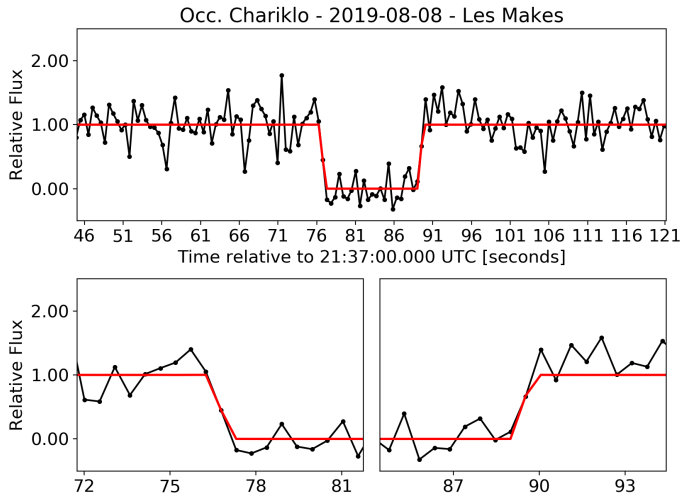
Fig. F.5. Light curve obtained at Les Makes on 2019-08-08.
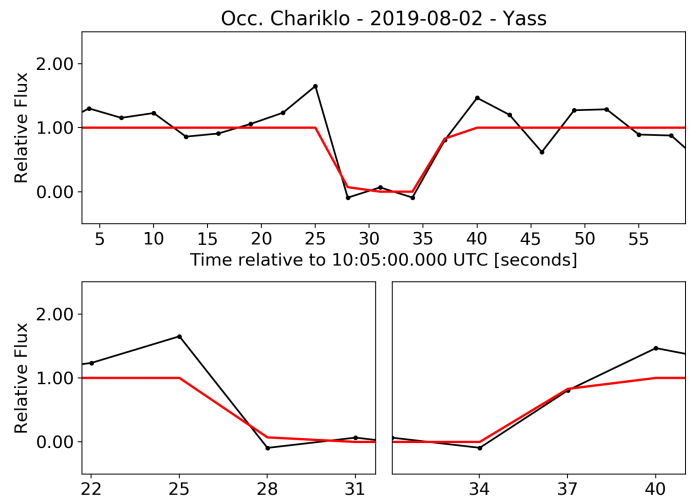
Fig. F.7. Light curve obtained at Yass on 2019-08-02.
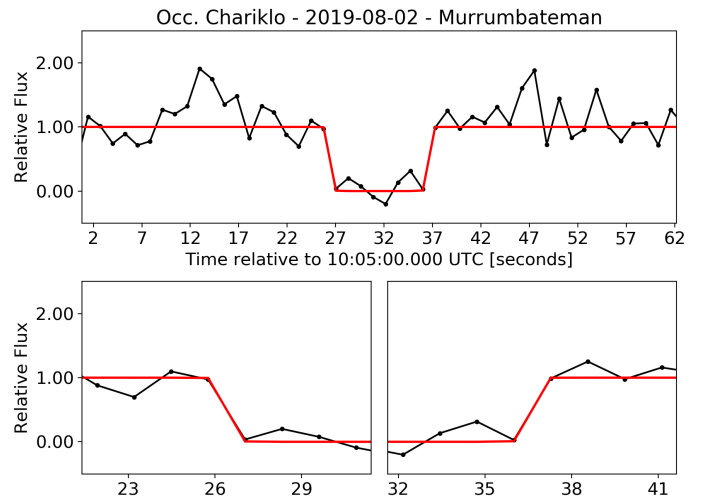
Fig. F.8. Light curve obtained at Murrumbateman on 2019-08-02.
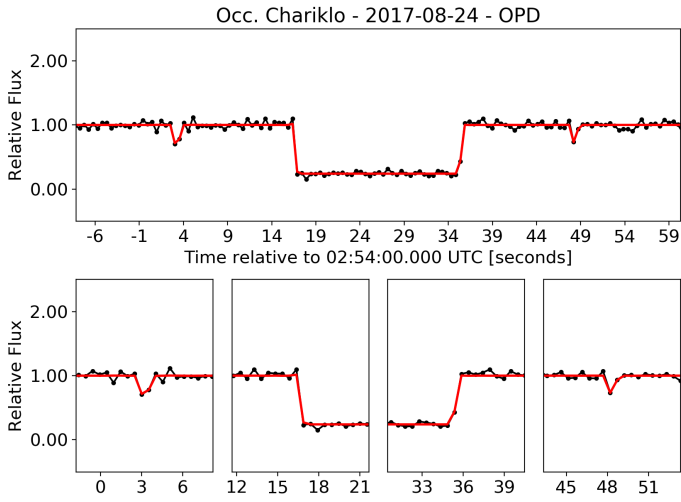
Fig. F.9. Light curve obtained at OPD on 2017-08-24.
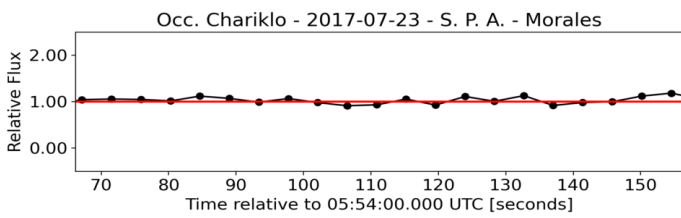
Fig. F.10. Light curve obtained at San Pedro de Atacama by Morales on 2017-07-23.
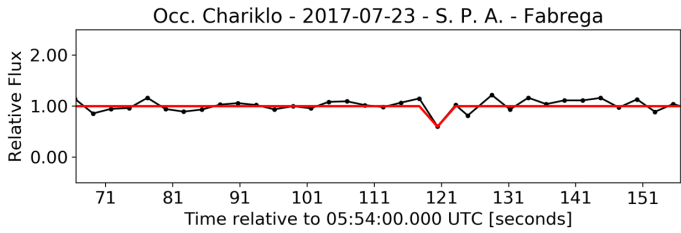
Fig. F.11. Light curve obtained at San Pedro de Atacama by Fabrega on 2017-07-23.
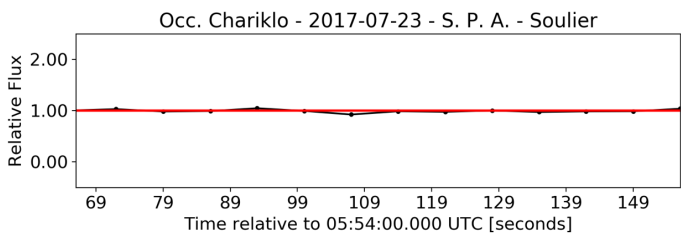
Fig. F.12. Light curve obtained at San Pedro de Atacama by Soulier on 2017-07-23.
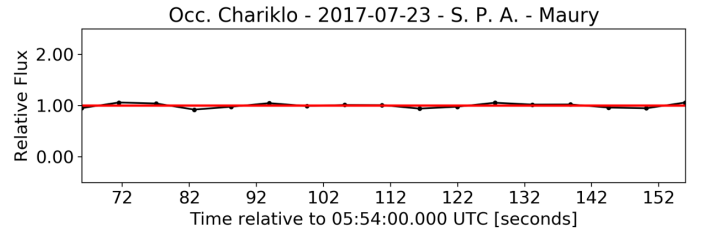
Fig. F.13. Light curve obtained at San Pedro de Atacama by Maury on 2017-07-23.
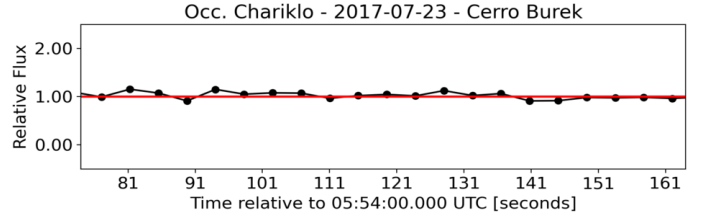
Fig. F.14. Light curve obtained at Cerro Burek on 2017-07-23.
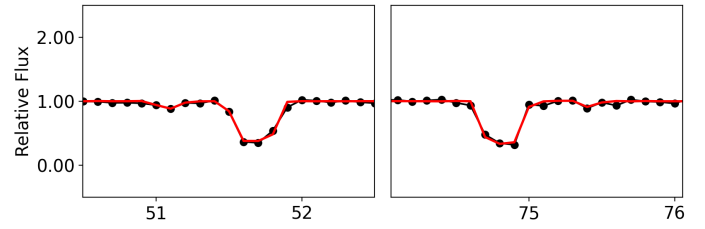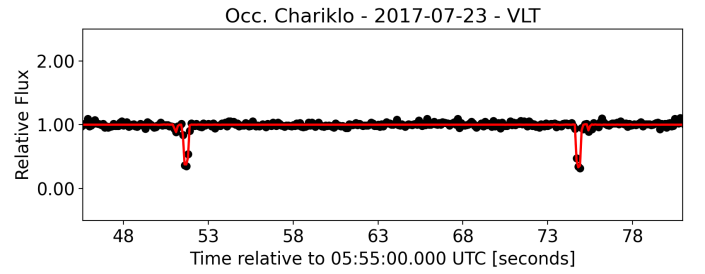
Fig. F.15. Light curve obtained at the VLT on 2017-07-23.
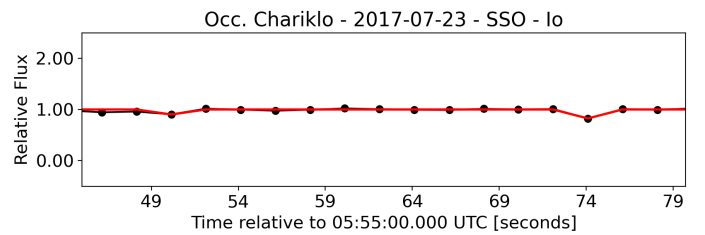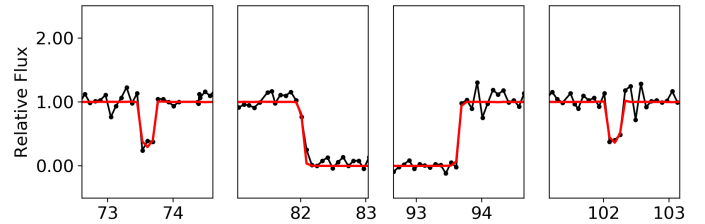

Fig. F.16. Light curve obtained at the SSO - Io on 2017-07-23.
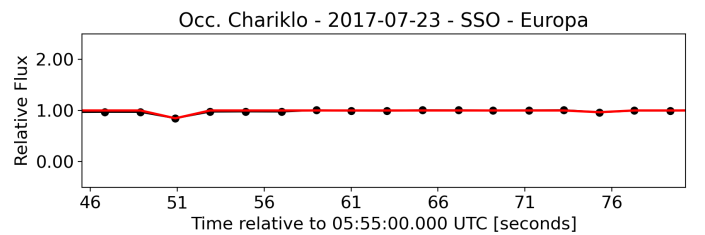
Fig. F.17. Light curve obtained at the SSO - Europa on 2017-07-23.
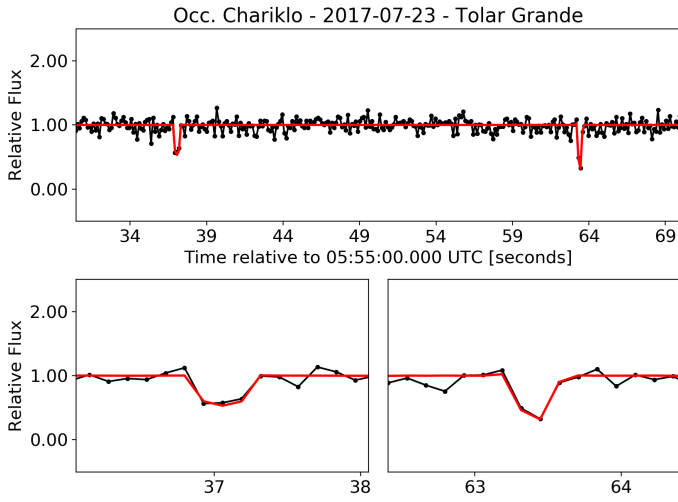
Fig. F.18. Light curve obtained at Tolar Grande on 2017-07-23.

Fig. F.19. Light curve obtained at Cono de Arita on 2017-07-23.

Fig. F.20. Light curve obtained at El Rodeo on 2017-07-23.

Fig. F.21. Light curve obtained at Cachi Adentro on 2017-07-23.

Fig. F.22. Light curve obtained at Augusto de Lima on 2017-07-23.
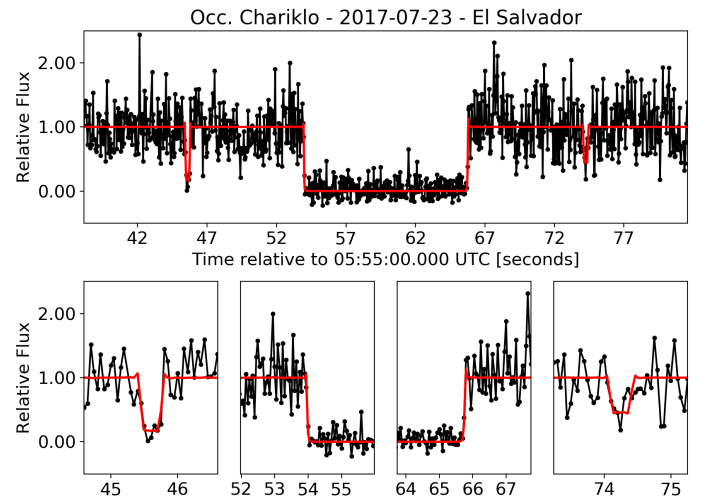
Fig. F.23. Light curve obtained at El Salvador on 2017-07-23.
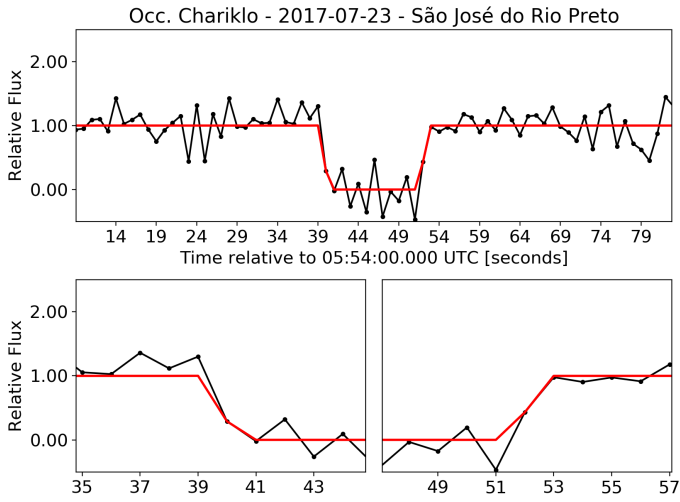
Fig. F.24. Light curve obtained at São José do Rio Preto on 2017-07-23.

Fig. F.25. Light curve obtained at Inca de Oro on 2017-07-23.

Fig. F.26. Light curve obtained at Bilac on 2017-07-23.

Fig. F.27. Light curve obtained with Danish with the Visual band on 2017-07-23.

Fig. F.28. Light curve obtained with Danish with the Red band on 2017-07-23.
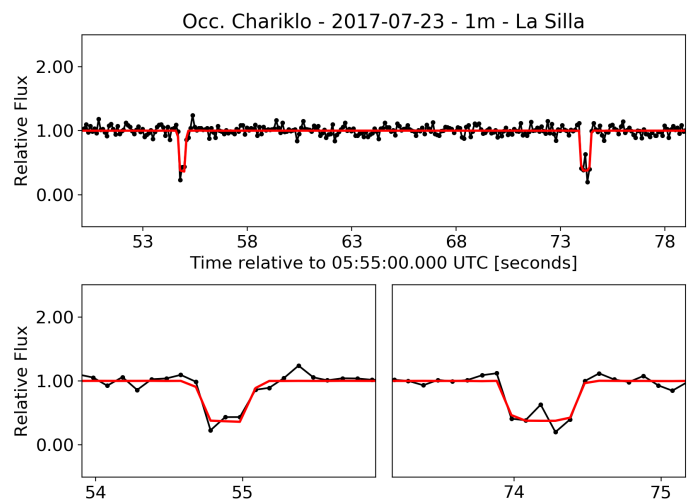
Fig. F.29. Light curve obtained with the 1m telescope in La Silla on 2017-07-23.
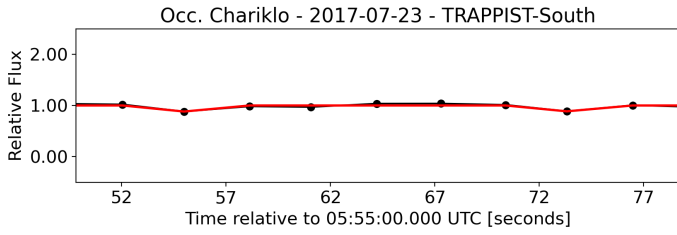
Fig. F.30. Light curve obtained with TRAPPIST-South on 2017-07-23.
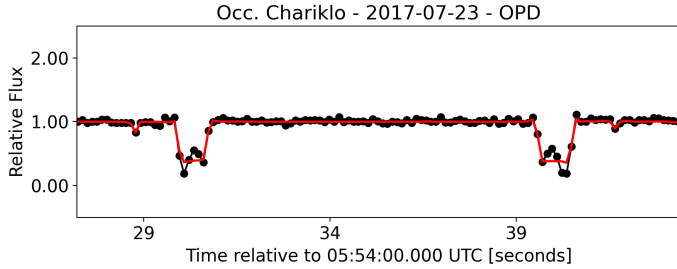
Fig. F.31. Light curve obtained at the OPD on 2017-07-23.
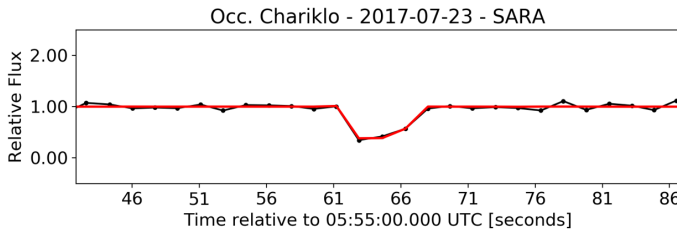
Fig. F.32. Light curve obtained with SARA on 2017-07-23.
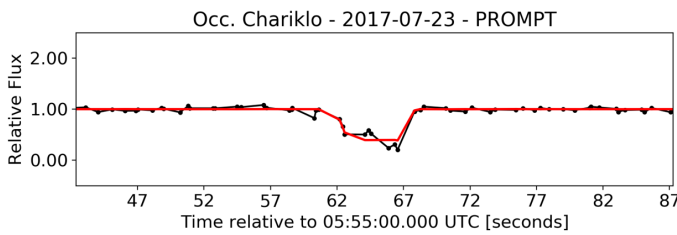
Fig. F.33. Light curve obtained with PROMPT on 2017-07-23.
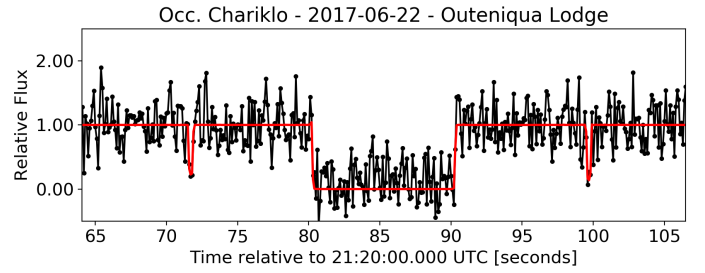
Fig. F.34. Light curve obtained at Outeniqua Lodge on 2017-06-22.
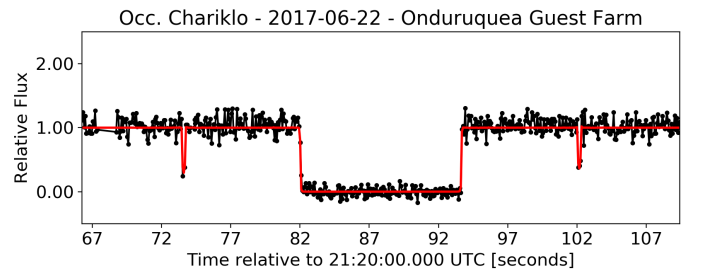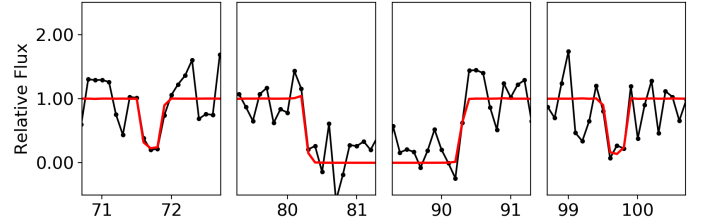
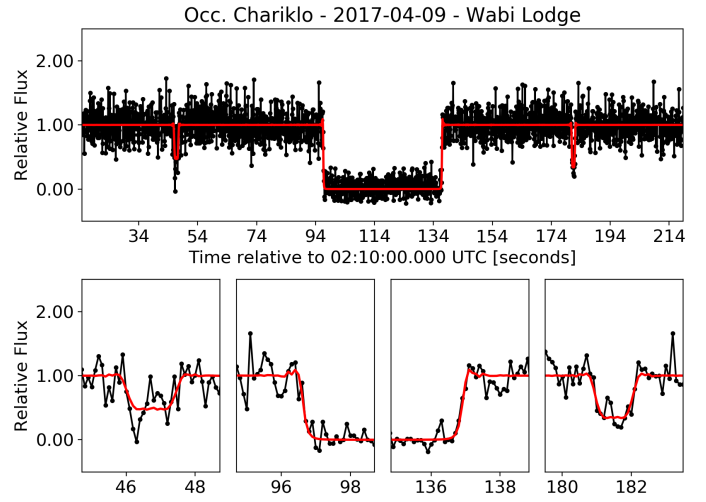**Fig. F.35.** Light curve obtained at Onduruquea Guest Farm on 2017-06-22.
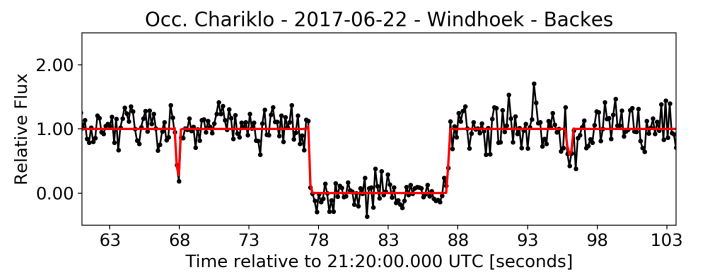
Fig. F.36. Light curve obtained at Windhoek by Backes on 2017-06-22.
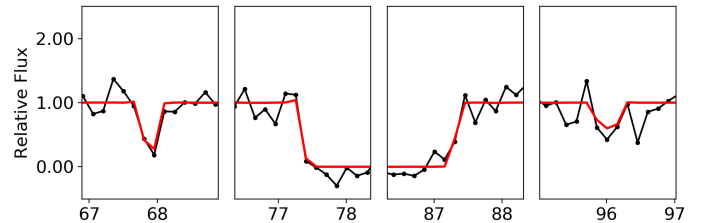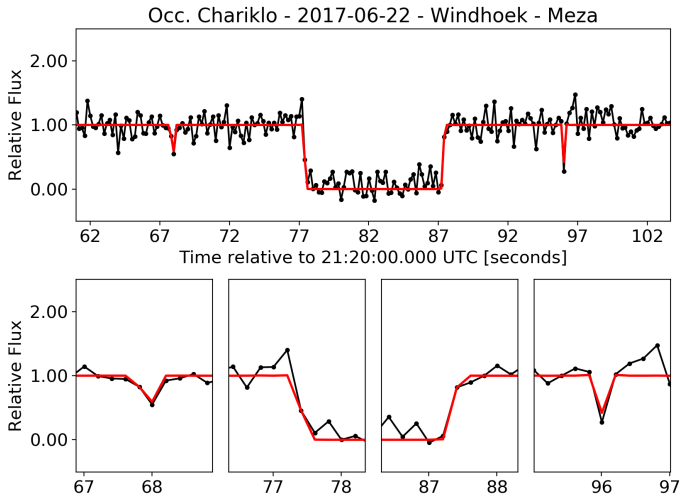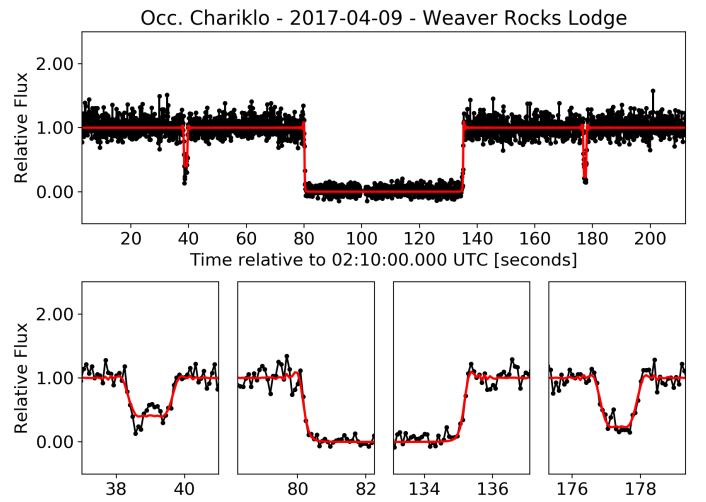
Fig. F.37. Light curve obtained at Windhoek by Meza on 2017-06-22.
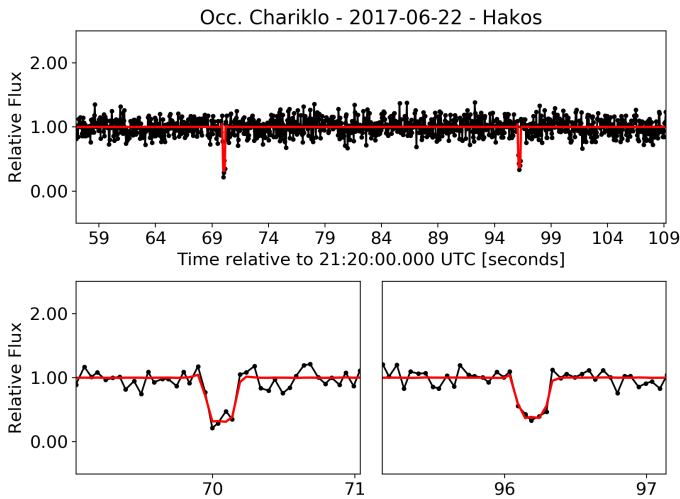

Fig. F.40. Light curve obtained at Wabi Lodge on 2017-04-09.
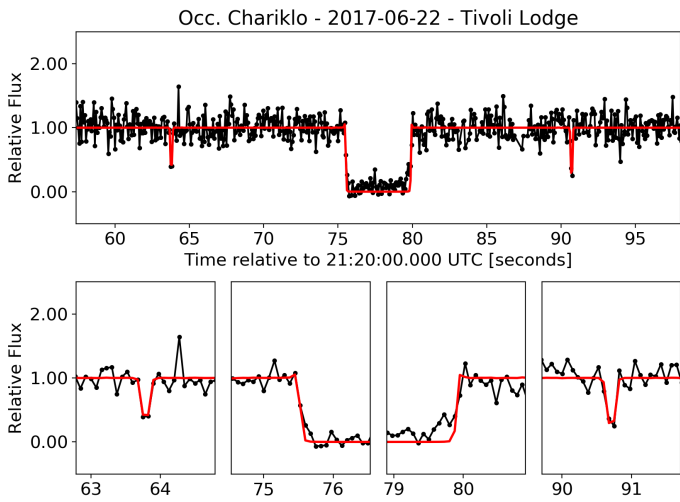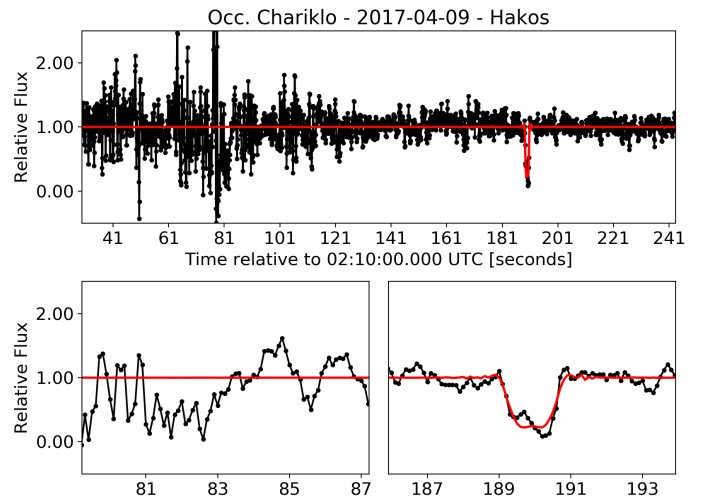

Fig. F.38. Light curve obtained at Tivoli Lodge on 2017-06-22.

Fig. F.41. Light curve obtained at Weaver Rocks Lodge on 2017-04-09.

Fig. F.39. Light curve obtained at Hakos on 2017-06-22.

Fig. F.42. Light curve obtained at Hakos on 2017-04-09.